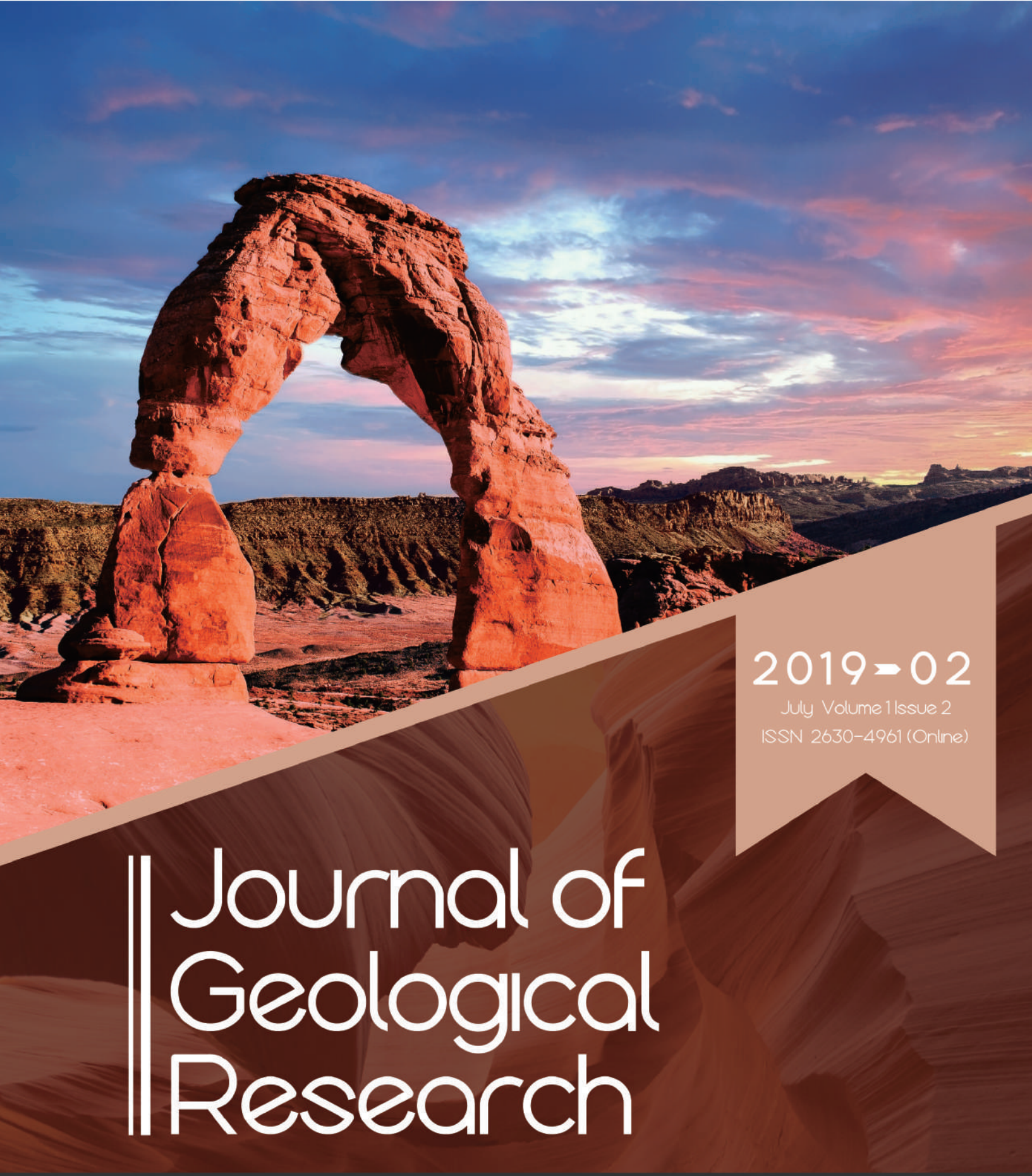

2019-02
July Volume 1 Issue 2
ISSN 2630-4961 (Online)

Journal of Geological Research

BILINGUAL PUBLISHING CO.
Pioneer of Global Academics Since 1984

Editor-in-Chief

Editorial Board Members

Volume 1 Issue 2 • July 2019 • ISSN 2630-4961 (Online)

Journal of Geological Research

BILINGUAL PUBLISHING CO.
Pioneer of Global Academics Since 1984

BILINGUAL PUBLISHING CO.
Pioneer of Global Academics Since 1984

Volume 1 | Issue 2 | July 2019 | Page 1-44
Journal of Geological Research

Contents

Article

Review

BILINGUAL PUBLISHING CO.
Pioneer of Global Academics Since 1984

Journal of Geological Research
https://ojs.bilpublishing.com/index.php/jgr-a

ARTICLE

Hydrocarbon Generation Potential Evaluation of Coal Shale Gas of Permo-Carboniferous in Jiyang Depression

Pingping Li[1] Huiyong Wang[2*] Shuanxiang Xu[3]

1. Shandong University of Science and Technology, Qingdao, 266590, China
2. Geophysical Research Institute of Shengli Oilfield Branch Co., Sinopec Dongying, 257022, China
3. Shandong XINJULONG Energy Co. Ltd, Heze, 274000, China

ARTICLE INFO

Article history
Received: 4 June 2019
Accepted: 12 August 2019
Published Online: 30 September 2019

Keywords:
Jiyang depression
Permo-Carboniferous
Shale gas
Hydrocarbon generation potential
Organic matter abundance

ABSTRACT

In order to study the hydrocarbon-generating potential of Carboniferous-Permian coal shale in Jiyang Depression, geochemistry, petroleum geology and coal geology were applied to study the residual strata distribution of Carboniferous-Permian in Jiyang Depression, organic matter abundance, organic matter types and organic matter maturity of mudstone. The results show that the thickness of the Carboniferous-Permian residual strata in Jiyang Depression is generally 200-800 m, with a maximum thickness of 900 m; the organic matter abundance of coal-bearing shale is good, and it is type III kerogen, which is conducive to gas generation, and the maturity of organic matter reaches a mature-higher maturity stage; the hydrocarbon generation potential of Benxi Formation and Taiyuan Formation is better; Medium to good hydrocarbon source rocks is able to be found in every sag of Shanxi Formation hydrocarbon source rocks, but the scope is limited, and the overall evaluation is still medium. Generally speaking, the Permo-Carboniferous coal-bearing shale in Jiyang Depression has certain shale gas exploration potential.

1. Introduction

Shale gas refers to natural gas in dark mud shale, which is mainly adsorbed and free. Essentially, it is a continuous generation of biochemical gas, thermogenic gas or a mixture of both [1-3]. The formation and distribution of shale gas have unique characteristics. Shale gas often distributed in the effective source rocks with large thickness and wide distribution in the basin, which has the advantage of large resource potential and long exploitation life [4-6]. Conventional wisdom holds that source rock can only produce oil and gas but cannot store oil and gas. However, with the development of times, it is gradually found that source rocks can not only generate natural gas but also store a large amount of natural gas [7-8]. Therefore, it is not too much to say that the formation of shale gas reservoirs is due to the adsorption of shale formation and hydrocarbon residue caused by low formation permeability [8]. However, cracks and voids in mud shale become the space where oil and gas occur, so a large part of the gas is retained in the mud shale stratum ("shale gas") [9].

The Jiyang Depression is located in the south of the Bohai Bay Basin. Where the Carboniferous-Permian is relatively developed. A large number of dark shales are

**Corresponding Author:*
Huiyong Wang,
Geophysical Research Institute of Shengli Oilfield Branch Co., Sinopec Dongying, 257022, China;
Email: Wanghuiyong2002@163.com

 DOI: https://doi.org/10.30564/jgr.v1i2.893

developed in Benxi Formation, Taiyuan Formation and Shanxi Formation, which are important source rocks because of their rich organic matter [10-13]. The Carboniferous-Permian sandstone reservoir in this area is object of exploration. Coal-derived gas from the Carboniferous-Permian coal-bearing source rocks was found in the Shihezi Formation sandstones [14], but the research on coal-bearing shale gas was relatively less. In this paper, the hydrocarbon generation potential of shale in Carboniferous-Permian in Jiyang Depression is studied by geochemical method, and the shale gas resource potential is determined, which has certain guiding significance for shale gas exploration in this area.

The abundance of organic matter is used to represent the relative content of organic matter in rocks, and to measure and evaluate the hydrocarbon generation potential of rocks. At present, there are three indicators to measure: the total organic carbon content (TOC), rock pyrolysis hydrocarbon generation potential (S1+S2) and hydrocarbon index (HI) [7-8, 10-15]. The hydrocarbon generation potential of shale in the Benxi, Taiyuan and Shanxi Formations has studied in detail. Among them, the Benxi Formation and the Taiyuan Formation are products of the epicontinental sea environment, while the Shanxi Formation is the formation of the deltaic environment [25]. Therefore, combining with sedimentary environment, the hydrocarbon generation potential of Benxi Formation and Taiyuan Formation and Shanxi Formation is discussed in this paper.

2. Regional Geological Survey

Jiyang Depression is a first-order negative tectonic unit, which converges westward and spreads eastward near east-west direction and is hosted by Chengning uplift and Luxi uplift in Bohai Bay Basin [13, 18]. It is bounded by Chengning uplift in the north, Luxi uplift in the south, Bohai Sea in the East and Linqing block fault basin in the west [11-13]. The depression includes Chezhen, Zhanhua, Huimin and Dongying sags [16] (Figure 1). The Carboniferous-Permian system in Jiyang Depression is similar to the whole North China area. In the late Ordovician of Early Paleozoic, due to the influence of Caledonian movement, the whole uplift was denuded, and the deposits of Upper Ordovician, Silurian, Devonian and Lower Carboniferous were missing. From the Late Carboniferous, the North China Platform was re-subsided and deposited, and a set of coal-bearing strata of marine-continental interaction was formed in the Late Permian. There are two sets of obvious sedimentary assemblages: from late Carboniferous to Early Permian, Jiyang Depression is a large epicontinental sea basin like North China. It deposited a set of "sea-land alternating" coal-bearing strata, that is, the main hydrocarbon-rich strata of Carboniferous-Permian. From early Permian to the end of Late Permian, Jiyang Depression is a large continental depression basin and has deposited a set of continental strata, which basically did not contain marine deposits and had poor coal-bearing property [17]. Thickness of the residual Carboniferous-Permian is generally 400-1000 m, and the maximum thickness is estimated to be about 1200 m. The thickness of dark mudstone and carbonaceous mudstone is 50-250 m. The maximum thickness of coal seam is 44.5m [18]. The coal-bearing strata in this area are Benxi Formation, Taiyuan Formation, Shanxi Formation, Lower Shihezi Formation and Upper Shihezi Formation[19-21]. Among them, Benxi Formation, Taiyuan Formation and Shanxi Formation are coal-bearing strata. The sedimentary environment of the Benxi Formation and the Taiyuan Formation is epicontinental marine environment, while the Shanxi Formation is formed in the river-controlled shallow water delta sedimentary environment [22].

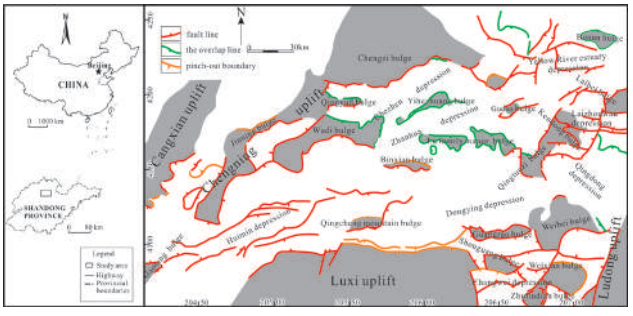

Figure1. Geographical location map of the study area and tectonic unit of Jiyang Depression

3. Coal-bearing stratum distribution

Jiyang Depression is relatively complete. From Archean to Cenozoic, except for the lack of Upper Ordovician, Silurian, Devonian and Lower Carboniferous, the rest of the strata are distributed in[23]. Carboniferous-Permian source rocks are abundant, mainly coal and dark mudstone[24]. Drilling data have confirmed that the Carboniferous-Permian strata are distributed in every depression of Jiyang Depression [25]. Drilling into the Carboniferous-Permian wells is mostly distributed in the Zhanhua sag and Chezheng sag in the north, while in the Dongying and Huimin sags in the south, relatively few wells are drilled in the Carboniferous-Permian coal measures. The distribution limit of the residual carboniferous-Permian strata in this area is controlled by the NE-trending faults developed in the late Mesozoic, which have the characteristics of North-South zoning or subdivision. They mainly distribute along the north-east direction on the slope of each depression to the sag belt. From north to south, they

DOI: https://doi.org/10.30564/jgr.v1i2.893

are Chexi-Dawang-Chengdong, Shaojia-Luojia-Gubei, Zizhen-Yangxin and Linnan. Lin Fanjia and Dongying Nanpo [26]. The coal-bearing strata of Carboniferous-Permian in Jiyang Depression are buried in depth of 500-7000 m, and the depth in most areas is 2000-6000m [14]. Residual thickness varies greatly in different locations. For example, the residual thickness in the southern and northern regions is generally 200-800m and the maximum thickness is 900m. According to the stratum thickness statistics of single well drilling, Qugu 2 well in Huimin sag has the largest stratum thickness, reaching 845 m, while Yigu 4 well in Zhanhua sag has the smallest stratum, only 9m. From the distribution of zones, the Chezhen Sag is mostly about 200m, with the maximum thickness of 642.5m (Chegu 31 well) and the minimum thickness of 25.5m (Chegu 11 well) (Figure 2); There are fewer Carboniferous-Permian drillings in Zhanhua sag, mainly concentrated in Shaojia-Luojia area, with the maximum thickness of 746 m and the minimum of 118 m. In the Dongying Depression, there are few exploration wells in the Carboniferous-Permian, and the distribution is uneven. The maximum drilling thickness is 623m, and the minimum is 23m; the maximum drilling thickness in Huimin sag is 845m and the minimum is 168m. According to the statistics of the drilled coal seam and the dark mudstone, the thickness of the coal seam is between 14-29 m, and the dark mudstone thickness is about 260 m.

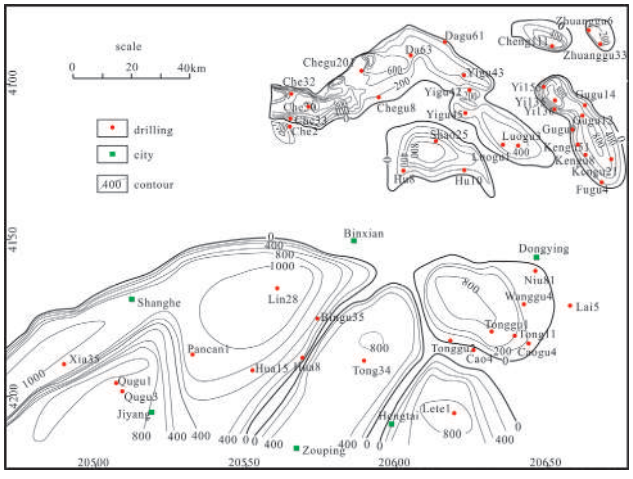

Figure 2. Stratum isopach map of Permo-Carboniferous in northeast of Jiyang Depression

4. Organic Geochemical Characteristics of Mud Shale and Evaluation of Source Rocks

4.1 Abundance of Organic Matter

Organic carbon (TOC) is the basis of hydrocarbon generation, and is also one of the important parameters reflecting the abundance of organic matter in shale [27]. It is also a key parameter for evaluating the source rock's gas generating capacity and gas production [28]. If the content of organic carbon is high, the ability of shale to generate hydrocarbon is strong, which mean that there are enough parent materials to generate hydrocarbons [29-30]. Hydrocarbon generation potential refers to the maximum amount of organic matter in a unit source rock that is able to be converted into hydrocarbons under natural geological conditions, usually expressed as S1 + S2. S1 indicates hydrocarbons that have been generated but not discharged from rocks, also known as residual hydrocarbons, and S2 indicates organic matter that is able to be generated but has not yet generated hydrocarbons in rocks [31].

4.1.1 Organic Matter Abundance of Benxi Formation and Taiyuan Formation

Most of the mudstones of Benxi and Taiyuan Formations in Dongying Depression have TOC less than 1.5%, S1+S2 less than 0.6 mg/g, and TOC and S1+S2 values in carbonaceous mudstones are higher, HI is 10-100, which generally belongs to poor gas source rocks.

The TOC of shale in Huimin Depression is generally 0.5% ~ 2.5%, and S1+S2 is generally 1 mg/g, up to 14.66 mg/g, generally medium-poor gas source rock.

Mudstones in Zhanhua sag are generally moderate to better gas source rocks. TOC in mudstone is generally greater than 1%, S1+S2 is mostly 0.5 ~ 4 mg/g, HI is lower, generally less than 100. Regionally speaking, TOC of Carboniferous in Luojia area is 0.6% ~ 1%, S1+S2 is basically less than 0.5%, and most of them are medium-poor gas source rocks with a Ro of 4% (Table 1). In the Yihezhuang area, the TOC of shale is generally 1% ~ 6%, S1+S2 is generally 1mg/g, the maximum is 15.32mg/g, and the maturity Ro is 0.8 ~ 1.35. It belongs to medium-good Source rock. The TOC of the Carboniferous mudstone in the Gubei area is high, ranging from 5% to 8%, and the maturity of Ro is 1.5% to 1.8%. It belongs to better gas source rock. (Table 1).

According to TOC, S1+S2, and HI frequency analysis, the TOC of mudstones in Benxi Formation and Taiyuan Formation is less than 4%, and the concentration distribution range is between 0.6% ~ 4%, which is medium-poor gas source rock (Figure 3). Among them, TOC was mainly 0.6%~1.5%, accounting for 49%, and the maximum peak value was 0.8%. S1+S2 is less than 3 mg/g, accounting for the vast majority, and is evaluated as medium-poor gas source rocks. The peak values of Benxi and Taiyuan Formations are about 0.1 mg/g, while those of Shanxi Formation are slightly better, about 0.6 mg/g. The HI is less than 100, and the medium-good source rock is about 40%. The

DOI: https://doi.org/10.30564/jgr.v1i2.893

overall assessment is medium-poor gas source rock. At the same time, the study also reveals that the mudstones of the Benxi and Taiyuan Formations are generally better in the north than in the south, while Dongying, Huimin, Chezhen and Zhanhua are better in turn (Table 1).

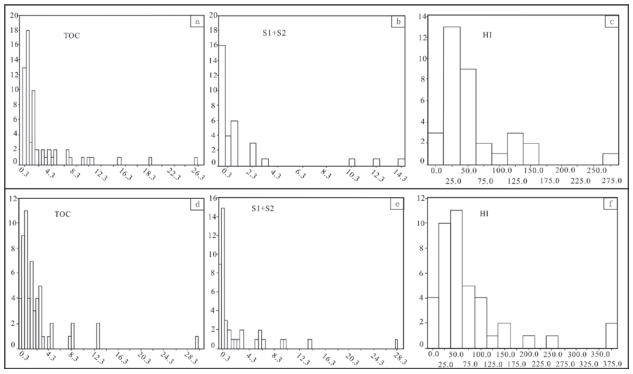

Figure 3. Frequency map of TOC S1+S2 HI of mudstones of Benxi and Taiyuan（a, b, c）、Shanxi（d, e, f） Formations in Jiyang Depression

Table 1. Geochemical characteristics of mud shale in Jiyang Depression

Position	Region	TOC%	S1+S2mg/g rock	HI	Maturity Ro	Evaluation
Benxi formation and Taiyuan formation	Dongying	<1.5	0.6	10-100	0.7-2.4	poor
	Huimin	0.5-2.5	0.3-1.5	40-60	0.8-2.2	middle-poor
	Zhanhua (Luojia)	0.6-1	<0.5	<40	4%	poor-middle
	Zhanhua (Yizhuang)	1-6	1-15.32	<100	0.8-1.35	middle-well
	Zhanhua(Isolated north)	5-8			1.5-1.8	preferably
Shanxi formation	Dongying	1.21-30.81	0.51-10.33	<100	1.0	middle-preferably
	Huimin	0.5-2.5	<1.5	30-60	1.1	middle-poor
	Chezhen				0.9	middle-preferably
	Zhanhua(Isolated north)	>1			maturity - migh maturity	middle-preferably
	Zhanhua (Isolated north)	0.8-3				middle

4.1.2 Organic Matter Abundance in Shanxi Formation

Carbonaceous mudstones are developed in Permian in Dongying Depression, with high TOC content ranging from 1.21% to 30.81%. TOC of carbonaceous mudstones is generally greater than 10%. S1+S2 is generally greater than 3 mg/g. Therefore, carbonaceous mudstones of Dongying Depression in Permian is a medium-fine gas source rock. (Table 1).

Permian TOC in Huimin sag is mainly 0.5%~2.5%, accounting for 70%. Grade distribution of effective gas source rocks: TOC mass fraction is less than 0.6%, accounting for 10%; TOC mass fraction is 0.6%~1.5%, accounting for 38%; TOC mass fraction is 1.5%~4.0%, accounting for 43%; TOC mass fraction is more than 4%, accounting for 9%. The hydrocarbon generation potential is mainly less than 1.5 mg/g, accounting for 88%. HI distributes mainly in the range of 30~60. The overall evaluation is medium-poor gas source rock (Table 1).

The Permian mudstones in the Chezhen sag has only been analyzed in Well Da 51, which is a medium-good gas source rock, slightly better than the underlying Carboniferous system (Table 1).

The TOC distribution area in Zhanhua sag is relatively wide, ranging from 0.5% to 6%, and S1+S2 is generally less than 2 mg/g. The evaluation is mainly medium gas source rocks. Each area in Zhanhua sag are different. The TOC of Permian mudstones in the Gubei area is generally more than 1%, with a maximum of 5.19%, and the maturity is also high. The peak temperature of pyrolysis is generally above 450°C and the highest temperature is 540°C. It is in the mature-high maturation stage. So most of them belong to medium-better gas source rocks. Among them, 54% are medium gas source rocks, better gas source rocks account for 15%, and the rest are poor gas source rocks. TOC in Gunan area is 0.8%~3%, which belongs to medium gas source rock (Table 1).

Generally speaking, the regularity of hydrocarbon source rocks in Shanxi Formation is not as good as that in Benxi Formation and Taiyuan Formation. Although medium-good hydrocarbon source rocks is able to be found in each depression, their scope is limited(Table 1).

Through TOC, S1+S2, and HI frequency analysis, it was found that TOC of source rocks in Shanxi Formation is generally less than 4%, and the main distribution range is 0.6%~4%. The peak value ranged from 0.6% to 1.5%, accounting for 37%. The distribution of S1+S2 is generally less than 4 mg/g and concentrated in the range of less than 1 mg/g. Among them, 22% were S1+S2 less than 0.5 mg/g, 43.9% were S1+S2 0.5-1.0 mg/g, and only 34% were others. The distribution of HI is generally less than 100. The proportion of medium- good source rock is about 40%, and that of poor source rock is about 50%. The overall evaluation is medium to poor source rocks.

4.2 Organic Type

Zhang Shanwen et al. [32] found that the whole background of the Bohai Bay Basin in the depositional period of the Benxi and Taiyuan Formations is the organic sedimentary facies of the shallow marsh forest, and that there were nearly East-

DOI: https://doi.org/10.30564/jgr.v1i2.893

West marsh forest sedimentary organic facies in the northern part of Jiyang Depression. During the sedimentary period of the Shanxi Formation, the Bohai Bay Basin developed mainly in the environment of delta, lagoon and tidal flat. The organic facies of shallow marsh forest deposits decreased significantly. The organic facies of terrestrial forest deposits developed in the northern part of Jiyang Depression and the organic facies of terrestrial forest deposits developed in the southern part of Jiyang Depression, while the organic facies of other deposits decreased significantly compared with Taiyuan formation, and the distribution range also decreased significantly. It is able to be concluded that the sedimentary organic facies of the Taiyuan Formation coal is much richer than that of the Shanxi Formation, and the hydrocarbon generation potential of the Taiyuan Formation coal is obviously better than that of the Shanxi Formation, and the matrix vitrinite and the crust composition of the Taiyuan Formation coal is better than that of the Shanxi Formation. The distribution map of organic elements in Jiyang area has been made. It is able to be found that the main type of organic matter in Carboniferous-Permian source rocks in Jiyang Depression is type III kerogen (Figure 4), which is mainly gas-generating source rocks.

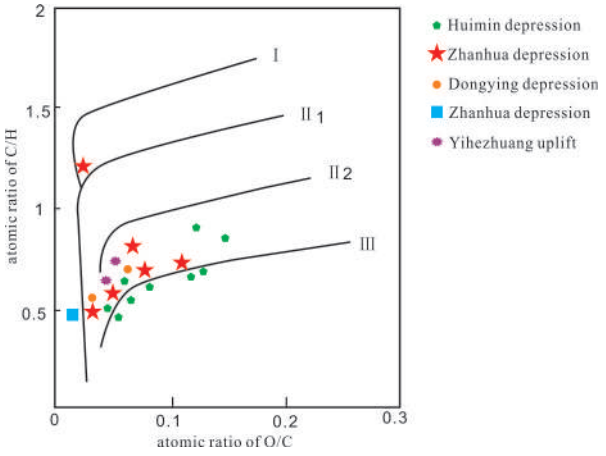

Figure 4. Organic elements distribution of coal series in Jiyang Depression

Table 2. Coal series maturity of Permo-Carboniferous in Jiyang Depression

region	depth (m)	Ro (%)
Chezhen-Dawangzhuang	2000-4000	0.62-0.72
Zhanhua Yidong	2000	0.63-0.9
Chezhen Zhuangxiqianshan	3500-4000	0.75-0.84
Zhanhua Isolated north	3700-5000	0.98-1.77
Zhanhua Island - Isolated north	2000-3100	0.65-0.87
Chezhen Luojia	3000-3400	1.18-1.48
Chezhen Wangpan town	2400-2700	0.75-1.05
Chezhen Qudi town	2400-3600	0.85-1.3

4.3 Organic Maturity

The maturity of organic matter plays an important role in shale gas formation. When the maturity is low (Ro < 0.6%), shale gas is mainly biogenic gas, or secondary biogas [33-34], which is formed by the biochemical decomposition of freshwater leaching after shallow burial. Biogenic gas and pyrolysis gas will be formed at the same time, and they are mixed shale gas with high and low maturity. When the maturity is high (1.1% < Ro < 2.0%), the shale gas mainly comes from the pyrolysis of organic matter and hydrocarbons, which is high maturity shale gas. When the thermal evolution degree of shale reaches over mature stage (Ro > 2.0%), shale gas is mainly dry gas of hydrocarbon pyrolysis.

The distribution of organic matter maturity RO of Carboniferous-Permian in Jiyang Depression is quite different, ranging from 0.6% to 5.16%. On the bulge and slope, the maturity of gas source rocks varies significantly among different regions. The Checheng-Dawangzhuang area has the lowest maturity, and the 4000m only reaches mature stage. In some areas, the maturity is high. For example, Gubei in Zhanhua, Luojia and Qudi in Chezhen, the maturation degree is higher, and Ro reach mature-high mature stage, which is related to the depth of burial (Table 2). From a flat point of view, the distribution trends of maturity of the Taiyuan Formation and the Shanxi Formation in the Bohai Bay Basin are consistent (Figure 5 and Figure 6). The Dongying sag is the main body, and the center of Zhanhua sag and Huimin sag are the high maturity centers, which distribute in a circular belt. Dongying sag is mainly in the high mature stage, Zhanhua sag and Huimin sag are mainly in the middle and late mature stage, while the western part is still in the mature stage.

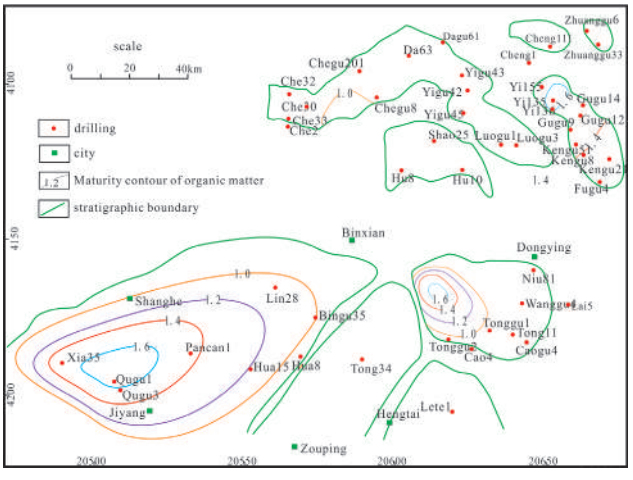

Figure 5. Contour line of organicmattermaturity of Benxi and Taiyuan Formations

DOI: https://doi.org/10.30564/jgr.v1i2.893

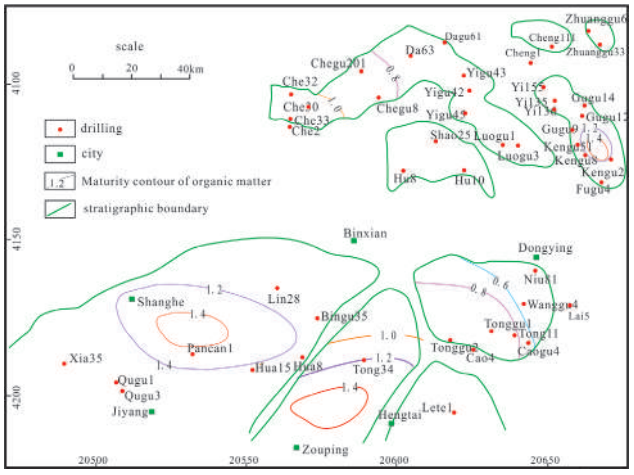

Figure 6. Contour line of organicmattermaturity of Shanxi Formation

5. Comparison of Hydrocarbon Generation potential of coal-bearing shale gas in Jiyang Depression

5.1 Stratigraphic Distribution Comparison

Compared with the large Carboniferous-Permian coal-forming gas fields (Suqiao-Wen'an, Dongpu and Wuqing) discovered in North China, the coal-bearing strata in Jiyang Depression are widely distributed, reaching 8700 km^2, second only to the Ordos Basin and the southern part of North China, but their stratigraphic continuity is poor. The stratum thickness is 200-800 m and belongs to the medium thickness stratum. Thus, the coal-bearing stratum conforms to the distribution characteristics of the existing Carboniferous-Permian coal-formed gas fields(Table 3).

5.2 Comparison of Shale Distribution and Maturity

The thickness of dark mudstone in Jiyang Depression ranges from 40 m to 100 m, with a maximum of over 300 m, and the thickness varies greatly. Most shales are buried in the depth of 900-8000 m, but generally more than 3 000 m, which belongs to the deep buried area. The maturity of shale is 0.6%~1.3%, which is lower than that of Dongpu, southern North China and Ordos Basin, but similar to that of Suqiao-Wen'an. In general, the shale in Jiyang Depression is deeply buried, and its maturity is similar to that in other depressions(Table 4).

5.3 Comparison of Shale Abundance

The organic matter abundance of the Carboniferous-Permian mudstones in Jiyang is at a medium level. TOC of shale is 0.5%~30.81%, which is generally greater than 1%. The hydrocarbon generation potential is 0.3-116.09 mg/g. Compared with other basins, the organic carbon content of mudstone in Jiyang Depression is in the middle level, and the hydrocarbon generation potential is relatively high, slightly lower than the Ordos Basin. Therefore, the Jiyang Depression has a certain potential for hydrocarbon generation in shale (Table 5)

Table 3. Mud shale characteristics of main gas field in our country

region	formation thickness (m)	distribution area (km^2)	distribution
Jiyang [14]	200-800	8700	part
Suqiao-Wenan [14]	700-1000	4564	part
Dongpu [14]	700-1000	5300	part
Wuqing [14]		2560	part
Southern north China[35]	600-900	31000	Part
Ordos Basin [36]		245800	continuous

Table 4. Mud shale characteristics of main gas field in our country

region	General mud shale thickness (m)	Maximum shale thickness (m)	cover depth(m)	maturity Ro(%)	Gas reservoir conditions
Jiyang [25]	50-100	300	900-8000	0.6-1.3	gas show
Suqiao-Wenan [25]	200-400	400	2600-4500	0.5-1.3	proven reserves 209×10^8 m^3
Dongpu [25]	100-160		1500-6000	0.8-2.0	proven reserves 480×10^8 m^3
Wuqing [25]	48-284		>3000	0.64-1.06	industrial gas flow
Southern north China [35]	300-400	600	1000-9000	0.8-3	
Ordos Basin [36]	60-200	200	600-5000	>2.0	Large gas fields

Table 5. Mudshale characteristics of main gas field in our country

region	organic carbon %	HI	S1+S2/(mg.g–1)
Jiyang [25]	0.5-30.81	30-100	0.3-116.09
Suqiao-Wenan [25]	0.1-26.9		0.02-77.9
Dongpu [25]	0.1-39.8		0.17-76.26
Wuqing[25]	0.1-38.8		0.02-82.06
Southern north China[35]	0.38-33.93	8.5-223.3	0.1-77.17
Ordos Basin [36]	0.05~23.38	212-266	94.7-204.1

In summary, compared with the shale characteristics of the main Carboniferous-Permian coal-formed gas fields

DOI: https://doi.org/10.30564/jgr.v1i2.893

in China, the hydrocarbon generation capacity of the Carboniferous-Permian coal-formed shale in Jiyang Depression is generally at a medium level, slightly higher than that in Puyang and South North China Basins, and has certain shale gas exploration potential.

6. Conclusion

(1) The Carboniferous-Permian residual strata in Jiyang Depression are thinner in the north and thicker in the south. The residual thickness is generally 200-800m, and the drilling thickness is up to 900 m. Due to the impact of the Mesozoic-Cenozoic fracture, the distribution of the Carboniferous-Permian strata in the northern part of Jiyang Depression is more obvious, and mainly distributed along the slopes of the sag to the sub-sag in the NE direction, and is distributed on five regional tectonic belts, from north to south, respectively for Chexi - Dawang - Chengdong, Shaojia - Luojia - Gubei, Zizhen - Yangxin, Linnan - Linfanjia, Dongying South Slope.

(2) Carboniferous-Permian coal rocks belong to better hydrocarbon source rocks. Type III kerogen of organic matter is conducive to gas generation. The maturity of organic matter reaches a mature-higher maturity stage and has the material basis for coal-bed methane generation. There are differences in the hydrocarbon generation potential of mudstones: Benxi Formation and Taiyuan Formation have better hydrocarbon generation potential in the northern part of the basin, that is, Dongying, Huimin, Chezhen and Zhanhua that become better in turn. And the regularity of hydrocarbon source rocks of Shanxi Formation is weaker than that of Benxi Formation and Taiyuan Formation. and medium-good hydrocarbon source rocks is found in each depression. However, the range is limited, and the overall evaluation is still moderate.

(3) Compared with other areas in China, the coal measures in Jiyang Depression are widely distributed and moderately thick. The organic matter abundance of Carboniferous-Permian mudstone is in the middle level, and the Carboniferous-Permian mudstone has certain hydrocarbon generation potential and exploration potential.

Acknowledge

This paper is completed under the careful guidance of teacher Lv Dawei. Professional knowledge, excellence in work style, rigorous academic attitude, tireless noble teacher ethics, strict self-discipline, generous manner, simple and approachable personality charm has far-reaching impact on me. I can't help but set up a lofty academic goal, master the basic research methods, and also make me understand a lot of the truth of dealing with people and people. From the topic selection to the completion of this paper, each step is newly completed under the guidance of the tutor, pouring a lot of effort into the tutor. Here I would like to express my great respect and heartfelt thanks to our guide.

References

[1] Curitis JB. Fractured shale2gas systems [J]. AAPG Bulletin, 2002, 86(11): 1921-1938.

[2] Ronaldj H, Daniel MJ, John Zumergeet et al. Oil and gas geochemistry and petroleum systems of the Fort Worth Basin[J]. AAPGBulletin, 2007, 91(4): 445-473.

[3] Bustin R.M. Gas shale tapped for big pay [J]. AAPG Explorer, 2005, 26(2):5-7.

[4] Cai-nneg Zou, Da-zhong Dong, She-xiao Wang et al. The formation mechanism, geological characteristics and resource potential of shale gas in China [J]. Petroleum exploration and development, 2010, 37(6): 641-653.

[5] Da-zhong Dong, Ke-ming Cheng, Yu-man Wang et al. Formation conditions and characteristics of lower Paleozoic shale gas in the upper Yangtze region of China [J]. Oil and natural gas geology, 2010, 31(3): 288-299.

[6] Li-dong Wang, Ming-de Zhang, Qing-hua Wu et al. Analysis on the possibility of shale gas resource storage in Jiyang Depression [J]. Shandong land and resources, 2016, 32(06): 27-31.

[7] Jin-xing Dai. Natural gas resources and their prospects of China [J]. Natural gas industry, 1999, 19(1): 3-6.

[8] Jin-chuan Zhang, Zhi-jun Jin, Ming-sheng Yuan. Formation mechanism and distribution of shale gas [J]. Natural gas industry, 2004, 24(7): 14-18.

[9] Yin, S., Ding, W.. Evaluation indexes of coalbed methane accumulation in the strong deformed strike-slip fault zone considering tectonics and fractures: A 3D geomechanical simulation study. Geological Magazine, 2018, 155: 1-17.

[10] Lin-ye Zhang, Li Zeng, Ri-Fang Zhu et al. The possibility of shale gas resources exists in the paleogene of Jiyang Depression [J]. Natural gas industry, 2008, 28(12): 26-20.

[11] Jia-sheng Yu, Pu-wei Wang, Yu-zhang Lin. Oil and gas resource potential in Qingdong sag [J]. Petroleum Geology and Recovery Efficiency, 2001, (5): 5-8.

[12] Pei-tong Shi, Xu-qing Fang, Chen Tao et al. Analysis of petroleum geological characteristics and exploration direction in Qingdong sag [J]. Journal of southwest petroleum university (natural science edition),

 DOI: https://doi.org/10.30564/jgr.v1i2.893

2009, 31(5): 43-48.
[13] Wen-jun Wang, Wei Li, De-yong Feng et al. Paleogene tectonic evolution and basin transformation in Qingdong sag [J]. Geotectonics and mineralogy, 2012, 36(1): 32-38.
[14] Shan-wen Zhang, Feng-gui Sui, Hui-xi Lin et al. Hydrocarbon geology and prospective evaluation of prepaleogene in bohai gulf basin [M]. Beijing geology press, 2008: 49-81.
[15] Bing-hai Wang, Kai Qian Ed. Geological research and exploration practice in shengli oil area [M]. Dongying in Shandong Province: University of petroleum press, 1992: 54-59
[16] Wei-lin Zhu, Guo-chun Wang. Analysis of reservoir forming conditions in Bohai shallow layer [J]. China Offshore Oil and Gas (geology), 2000, 14 (6): 367-374.
[17] Hai-peng Yao. Effective Source Rock of Permo-carboniferous Coal Measure Taiyuan Formation in Jiyang Depression [J]. Shanxi Coal, 2015, 35(02): 4-7.
[18] Zheng Li. Hydrocarbon-generation evolution of Permian-Carboniferous source rock in Jiyang Depression. Journal of Petroleum [J]. 2006(04): 29-35.
[19] Hui-li Wang, Wei-feng Wang, Wang Xin. Preliminary exploration of paleogene seismic facies and sedimentary facies in Qingdong sag [J]. Journal of petroleum and natural gas, 2009, 31(5): 250-254.
[20] Zheng Huang, Zhi-ping Wu, Wei Li et al. Vertical stratigraphic sequence and distribution characteristics of Cenozoic strata in qingdong sag [J]. Geological Journal of China Universities, 2010, 16(1): 94-102.
[21] Wei Wang, Kui Wu, Zhong-qiao Zhang, et al. Reservoir diagenesis and pore evolution in shahejie formation of Qingdong sag. Mineral and rock, 2012, 32(3): 94-102.
[22] Zeng-xue Li, Zhong-xiang Cao, Zhen-ming Wang et al. The burial conditions of carboniferous Permian in Jiyang Depression and the distribution characteristics of coal-type gas source rocks [J]. Coal geology and prospecting, 2004, 32(4): 4-6.
[23] Shandong coal field geological exploration company. Regularity of coal accumulation and coal prospecting in late Paleozoic in north China (Sedimentary thematic research report of shandong part) [R]. 1990.
[24] Lin-ping Yu, Zhong-xiang Cao, Zeng-xue Li. Organic geochemical characteristics of carboniferous Permian source rocks in Jiyang Depression [J]. Geology – Geochemistry, 2003, 31(4): 68-73.
[25] Jin Liu, Yu-liang Liu, Hong-han Chen et al. Analysis of main control conditions of coal gas accumulation in linnan area [J]. Petroleum Geology and Recovery Efficiency, 2002, 9(4): 42-44.
[26] De-lin Zhang Ed. Principle and practice of seismic data oil and gas display research [M]. Beijing: Petroleum Industry Press, 2000:142-145.
[27] Ling Liu, Feng Wang, Da-zhen Tang et al. Evaluation on Upper Paleozoic Coal-Bearing Source Rocks and Hydrocarbon Expulsion Feature in Linxing Region [J]. Special Oil and Gas Reservoirs , 2018, 25(1): 5-10.
[28] Qi-qi Li, Bin Li, Yi-ling Liu et al. Paleozoic Source-Rock Properties and Hydrocarbon Generation Potential in Northwest Sichuan [J]. Special Oil and Gas Reservoirs, 2018, 25(3): 45-49.
[29] Wei-chi Zeng, Jin-chuan Zhang, Wen-long Ding et al. The Gas Content of Continental Yanchang Shale and Its Main Controlling Factors: A Case Study of Liuping-171 Well in Ordos Basin [J]. Natural Gas Geoscience, 2014, 25(2): 291-301.
[30] Wen-quan Peng, Yong-biao Lian. Study on Influential Factors of Shale Gas Content in Non-marine Sedimentary Basins——Setting Weibei Sag as an Example [J]. Land and Resources of Shandong Province, 2017, 33(7): 25-30.
[31] Gu Gong, Chun-chi Zhang, Bing-yan Gao. Study on Upper Paleozoic Shale Gas Reservoiring Condition in Western Shandong [J]. Coal geology in China, 2018, 30(10): 43-48.
[32] Shan-wen Zhang, Lin-ye Zhang, Zheng Li. The process of coal gas accumulation in gubei buried hill of Jiyang Depression analysis [J]. Natural Gas Geoscience, 2009, 20(5): 670 – 677.
[33] Curtis J B. Fractured shale gas systems[J]. AAPG Bulletin, 2002, 86(11): 1921-1938.
[34] Martini A M, Walter L M, Ku T C W, et al. Microbial production and modifycation of gases in sedimentary basins: A geochemical case study from a Devonian shale gas play, Michigan basin[J]. AAPG Bulletin, 2003, 87(8):1355-1375.
[35] Xiao-yun Lin, Qian-lan Chen, Jing Li. Distribution and geochemistry of Permian source rocks in north China [J]. Marine geologic front, 2011, 27(4): 21-25.
[36] Xiao-yan Li, Shen-li Si. The potential of coal pyrolysis and hydrocarbon generation in ordos basin [J]. Coal geology and prospecting, 2008, 36(3): 1-11.

DOI: https://doi.org/10.30564/jgr.v1i2.893

BILINGUAL PUBLISHING CO.
Pioneer of Global Academics Since 1984

Journal of Geological Research
https://ojs.bilpublishing.com/index.php/jgr-a

ARTICLE

3D Gravity Inversion with Correlation Image in Space Domain and Application to the Northern Sinai Peninsula

Xu Zhang[1] Peng Yu[2] Jian Wang[3*]

1. Shanghai Shannan Investigation & Design Co.,Ltd. , Shanghai, 201206, China
2. State Key Laboratory of Marine Geology, Tongji University, Shanghai, 200092, China
3. Key Laboratory of Crustal Dynamics, Institute of Crustal Dynamics, China Earthquake Administration, Beijing, 100085, China

ARTICLE INFO

Article history
Received: 15 May 2019
Accepted: 3 June 2019
Published Online: 30 July 2019

Keywords:
3D gravity inversion
Space domain
Correlation image
Effective equivalent storage
Subdomain technique
Northern Sinai Peninsula

ABSTRACT

We present a 3D inversion method to recover density distribution from gravity data in space domain. Our method firstly employs 3D correlation image of the vertical gradient of gravity data as a starting model to generate a higher resolution image for inversion. The 3D density distribution is then obtained by inverting the correlation image of gravity data to fit the observed data based on classical inversion method of the steepest descent method. We also perform the effective equivalent storage and subdomain techniques in the starting model calculation, the forward modeling and the inversion procedures, which allow fast computation in space domain with reducing memory consumption but maintaining accuracy. The efficiency and stability of our method is demonstrated on two sets of synthetic data and one set of the Northern Sinai Peninsula gravity data. The inverted 3D density distributions show that high density bodies beneath Risan Aniza and low density bodies exist to the southeast of Risan Aniza at depths between 1~10 and 20 km, which may be originated from hot anomalies in the lower crust. The results show that our inversion method is useful for 3D quantitative interpretation.

1. Introduction

3D gravity inversion is vital to quantitative interpretation of the Earth's interior compositions and structures. However, gravity inversion is never unique due to the ubiquitous presence of observation errors and the inherent source ambiguity of the gravity potential [20]. Numerous imaging methods for potential field data have been proposed to estimate source parameters. Patella [22] presented a probability inversion method which was applied to gravity data by Mauriello and Patella [19]. Guo et al. [10,20] proposed the correlation image method based on the study of probability images, which produced a higher resolution of density/magnetization distribution by using the vertical gradient of potential data. Fedi [7,8] presented Depth from Extreme Points (DEXP) method and demonstrated that the resulting image was equivalent to a weighted upward continuation of potential fields by comparing with other methods. Baniamerian et al. [3,4] proposed a variant of the DEXP method, which generated an image of a quantity proportional to the source distribution. Chauhan et al.[6] de-

**Corresponding Author:*
Jian Wang,
Key Laboratory of Crustal Dynamics, Institute of Crustal Dynamics, China Earthquake Administration, Beijing, 100085, China;
Email: wangjianhydz@163.com

 DOI: https://doi.org/10.30564/jgr.v1i2.845

scribed an accurate method for performing upward continuation and vertical differentiation in space domain. Because the methods are all noniterative, stable, and convenient in calculation, they are touted as providing useful starting model for 3D inversion [8,9].

Forward calculations for potential field are mainly divided into space- and frequency-domains. Space domain methods provide closed-form equations to calculate potential fields directly and accurately. However, when large number of field data is to be modeled, space domain solutions are considerably slow. Frequency domain methods are simpler and faster by using the Fast Fourier Transform, but they have been plagued by imposed periodicity and edge effect (e.g. [5]).

There are two basic methods to partly overcome the problems of the great cost of computational time and memory footprint in the space domain processing and interpretation: (1) fast calculation of forward modeling, and (2) reducing the number of inversion iterations on the basis of maintaining accuracy. Portniaguine and Zhdanov [23,29] proposed a compression technique based on cubic interpolation for decreasing computer memory and accelerating the calculation speed. Li and Oldenburg [16] introduced a wavelet transform to compress the sensitivity matrix and improved the efficiency of forward modeling. Yao [27] presented an equivalent storage technique based on the equivalence and interchangeability of potential field to inverse gravity and magnetic anomalies for 3D physical properties. Yao et al. [28] proposed a stochastic subspace technique to reduce the number of inversion dimensions. Shamsipour et al. [24,25] presented stochastic inversion to reduce the number of inversion iterations. Abedi et al. [2] applied a bidiagonal matrix with favorable lower dimensions to increase the speed of the algorithm. MohammadRezaie et al. [18] combined the Krylov method with a regularization method applied to the low-dimensional projected problem.

In this work, we present a 3D gravity inversion with correlation image in space domain. Firstly, we take the 3D correlation image of the vertical gradient of gravity data (CIVG) as a starting model to generate a smooth image. Secondly, we use effective equivalent storage and subdomain techniques to increase the computational speed of forward modeling. Thirdly, 3D density distributions are obtained by inverting CIVG to fit the synthetic/field data using the steepest descent method. Because the effective equivalent storage and subdomain techniques are utilized to the starting model calculation of the forward modeling and the inversion, all these processes can be carried out fast in space domain with reducing memory consumption but maintaining accuracy. We further verify the feasibility and stability of the method by applying on the field data of the Northern Sinai Peninsula.

2. Methodology

2.1 Gravity Data and Its Vertical Gradient Correlation Image

Guo et al. [10] presented a correlation image method for gravity data and its vertical gradient on regular gridded data. Suppose that the z-axis is positive downwards, and the observation plane is at zero level. The gravity anomaly caused by an arbitrary cell q with volume V can be expressed as

$$g\left(x_i, y_i\right) = GV\Delta\sigma_q B_q\left(x_i, y_i\right), \text{ *MERGEFORMAT (1)}$$

where G is the Newton's gravitational constant, $\Delta\sigma_q$ is the density contrast between the anomalous body and background mass, and $B_q\left(x_i, y_i\right)$ is a geometrical function

$$B_q\left(x_i, y_i\right) = \frac{z_q}{r\left(x_i, y_i\right)^3}, \text{ *MERGEFORMAT (2)}$$

here $r\left(x_i, y_i\right) = \left[\left(x_q - x_i\right)^2 + \left(y_q - y_i\right)^2 + z_q^2\right]^{1/2}$, $\left(x_i, y_i\right)$ is the observation point at sea level, and $\left(x_q, y_q, z_q\right)$ is the source point.

The normalized correlation between the observed and forward data is calculated as follow [10]

$$C_q\left(x_q, y_q, z_q\right) = \frac{\sum_{i=1}^{N} \Delta g\left(x_i, y_i\right) \Delta g_q\left(x_i, y_i\right)}{\sqrt{\sum_{i=1}^{N} \Delta g^2\left(x_i, y_i\right) \sum_{i=1}^{N} \Delta g_q^2\left(x_i, y_i\right)}},$$

*MERGEFORMAT (3)

where $\Delta g\left(x_i, y_i\right)$ is the observation data, $C_q\left(x_q, y_q, z_q\right)$ is the coefficient of normalized correlation, and N is the total number of observation points. If $\Delta\sigma_q$ is positive, Eq. (3) can be simplified to

$$C_q\left(x_q, y_q, z_q\right) = \frac{\sum_{i=1}^{N} \Delta g\left(x_i, y_i\right) B_q\left(x_i, y_i\right)}{\sqrt{\sum_{i=1}^{N} \Delta g^2\left(x_i, y_i\right) \sum_{i=1}^{N} B_q^2\left(x_i, y_i\right)}},$$

*MERGEFORMAT (4)

and according to the Cauchy inequality, we can obtain

$$-1 \le C_q\left(x_q, y_q, z_q\right) \le 1. \text{ *MERGEFORMAT (5)}$$

CIVG can also be expressed in the same way

DOI: https://doi.org/10.30564/jgr.v1i2.845

$$C_{q,z}\left(x_q, y_q, z_q\right)=\frac{\sum_{i=1}^{N}\Delta g_z\left(x_i, y_i\right)B_{q,z}\left(x_i, y_i\right)}{\sqrt{\sum_{i=1}^{N}\Delta g_z^2\left(x_i, y_i\right)\sum_{i=1}^{N}B_{q,z}^2\left(x_i, y_i\right)}},$$

*MERGEFORMAT (6)

in which $\Delta g_z\left(x_i, y_i\right)$ is the vertical gradient of the observation data, and $B_{q,z}\left(x_i, y_i\right)$ is the vertical gradient of $B_q\left(x_i, y_i\right)$, which is also a geometrical function

$$B_{q,z}\left(x_i, y_i\right)=\frac{2z_q^2-\left(x_q-x_i\right)^2-\left(y_q-y_i\right)^2}{\left[\left(x_q-x_i\right)^2+\left(y_q-y_i\right)^2+z_q^2\right]^{5/2}}=\frac{3z_q^2-r^2}{r^{5/2}}.$$

*MERGEFORMAT (7)

The correlation image of either the gravity anomaly or the vertical gradient is equivalent to a weighted upward continuation reflecting the density distribution characteristics. Therefore, CIVG is considered as a useful starting model for the subsequent 3D inversion, which can reduce non-uniquencess, uncertainty and the number of iterations.

2.2 Equivalent Storage Technique

Yao [27] proposed an equivalent storage technique based on the equivalence of shift and the symmetry reciprocation of potential field (Figure 1). From Eq. (2), we can see that the geometrical function is only determined by the distances from the centers of cells to the observation points, when the sources locating within one layer. Take the first layer as an example, the distance from the first grid of this layer to the first observation point is equal to the distance from an arbitrary grid of the layer to its corresponding observation point (Figure 1a), which can be written as [27]

$$B_{(1,1,1)}\left(1,1\right)=B_{(1,2,1)}\left(1,2\right)=\cdots=B_{(i,j,1)}\left(i,j\right)=\cdots=B_{(m,n,l)}\left(m,n\right),$$

*MERGEFORMAT (8)

here $B_{(i,j,1)}\left(i,j\right)$ is the geometrical function of Eq. (2), the subscript $\left(i,j,1\right)$ is the source points, $\left(i,j\right)$ is the observation point at sea level, and $\left(m,n\right)$ is the size along the x - and -directions. According to the plane geometry theory, the segments sandwiched between two parallel planes are equals, and then Eq. (8) can be extended to

$$B_{(1,1,1)}\left(k,l\right)=\cdots=B_{(i,j,1)}\left(i+k-1,j+l-1\right)=\cdots=B_{(m-k+1,n-l+1,1)}\left(m,n\right).$$

*MERGEFORMAT (9)

Based on Eq. (9), the geometrical function of an arbitrary point can be replaced by the first point on the same layer. The interchangeability of the geometrical functions can be written as

$$B_{(1,1,1)}\left(k,l\right)=B_{(k,l,1)}\left(1,1\right)=\cdots=B_{(i+k-1,j+l-1,1)}\left(i,j\right)=B_{(i,j,1)}\left(i+k-1,j+l-1\right),$$

*MERGEFORMAT (10)

combining Eq. (9) with Eq. (10), we obtain

$$B_{(i,j,1)}\left(k,l\right)=B_{(1,1,1)}\left(\left|i-k\right|+1,\left|j-l\right|+1\right).$$ *MERGEFORMAT (11)

Figure 1 is the sketch map showing the distances between the sources and observation points used for equivalent storage technique. When grid meshing has been suitably established, the geometry of gridding is fixed in the iterative inversion. We can then employ the equivalent storage technique to relax the demand on computer memory and increase the computational efficiency. It is worth mentioning that the technique works when the gridding of 3D domain along the x - and y -directions is the same as that used for the observation plane.

2.3 Subdomain Technique

To further increase the computational speed and reduce the memory usage, we propose a technique of subdomain in this section. We calculated the gravity anomaly by an infinitely extended line along the x -axis with depth z_q from gridded data. We assume a line segment length a with density σ, the outline length 2(b-a) with density $k\sigma$, here b is infinity, and k is constant. The gravity anomaly above the center of line segment can be expressed as

$$\Delta g=G\sigma v_q\int_{-a}^{a}\frac{z_q}{r\left(x_i, y_i\right)^3}dx=G\sigma v_q\int_{-a}^{a}\frac{z_q}{\left(\left(x_q-x_i\right)^2+z_q^2\right)^{3/2}}dx$$

$$=G\sigma v_q\left[\frac{a}{z_q\sqrt{a^2+z_q^2}}-\left(\frac{-a}{z_q\sqrt{a^2+z_q^2}}\right)\right]=G\sigma v_q\frac{2a}{z_q\sqrt{a^2+z_q^2}}.$$

*MERGEFORMAT (12)

Then the ratio of the gravity anomalies between the whole line and the line segment can be expressed as

$$\frac{\Delta g_2}{\Delta g_1}=\frac{Gk\sigma v_q\frac{2(b-a)}{z_q\sqrt{b^2+z_q^2}}-G\sigma v_q\frac{2a}{z_q\sqrt{a^2+z_q^2}}}{G\sigma v_q\frac{2a}{z_q\sqrt{a^2+z_q^2}}}$$

$$=\frac{Gk\sigma v_q\frac{2b}{z_q\sqrt{b^2+z_q^2}}-G(k-1)\sigma v_q\frac{2a}{z_q\sqrt{a^2+z_q^2}}}{G\sigma v_q\frac{2a}{z_q\sqrt{a^2+z_q^2}}}$$

$$=\frac{k\left(\frac{2b}{z_q\sqrt{b^2+z_q^2}}-\frac{2a}{z_q\sqrt{a^2+z_q^2}}\right)}{\frac{2a}{z_q\sqrt{a^2+z_q^2}}}+1=k\frac{b\sqrt{a^2+z_q^2}-a\sqrt{b^2+z_q^2}}{a\sqrt{b^2+z_q^2}}+1,$$

*MERGEFORMAT (13)

DOI: https://doi.org/10.30564/jgr.v1i2.845

Because b is infinity number, we can obtain

$$\frac{\Delta g_2}{\Delta g_1} = k\frac{b\sqrt{a^2+z_q^2}-ab}{ab}+1 = k\left(\sqrt{1+\left(\frac{z_q}{a}\right)^2}-1\right)+1 ,$$

*MERGEFORMAT (14)

assuming $a = 20z_q$, and $k = 10$, then

$$\frac{\Delta g_2}{\Delta g_1} = 10\left(\sqrt{1+\left(\frac{1}{20}\right)^2}-1\right)+1 = 10\times 0.001+1 = 1.01 .$$

*MERGEFORMAT (15)

Eq. (15) implies that the subdomain technique is an approximate quantitative determination method to reduce the computational time of forward modeling with a high fitting accuracy. Due to the line is arbitrary, and all other lines can be applied in the same layer, this technique can be extended to the entire plane.

Here we take an example to illustrate the efficiency of the combined techniques of equivalent storage and subdomain. A 3D domain is divided into $1000\times 1000\times 10$ cubic prisms with a grid spacing of 1, and the observation data are also calculated on a 1000×1000 grid with an interval of 1. The storage of a geometrical function is 10^{13} without using the equivalent storage technique, whereas the storage is 10^7 if using the equivalent storage technique. With the subdomain technique, the storage can be further reduced to be 10^5.

2.4 The Steepest Descent Inversion Method

The conventional way of solving ill-posed inverse problems is based on the misfit functional determined as a norm of difference between the observed and theoretical data

$$p(m,d) = \left\|A(m)-d\right\|^2 = \min ,$$ *MERGEFORMAT (16)

where, A is the forward modeling operator, d is the observation data.

In this study, we apply the steepest descent method to inverse the 3D density distribution. One iteration step, from iteration number n to number n+1, can be summarized as follows [30]

$$\begin{aligned} r_n &= A(m_n)-d \\ I_n &= A^T r_n \\ s_n &= AI_n \\ k_n &= \left\|s_n\right\|^2 / \left\|I_n\right\|^2 \\ m_{n+1} &= m_n - k_n I_n , \end{aligned}$$ *MERGEFORMAT (17)

where I_n is the steepest descent direction, k_n is the step length in the direction, r_n is the residual between the observed and theoretical data.

2.5 Inversion Strategy

The following is a summary of the inversion strategy we used to apply correlation image theory and effective equivalent storage and subdomain techniques to obtain 3D density distribution (Figure 2):

(1) we calculate the geometrical function of the point located in the first row and the first column of the 3D domain using Eqs. (2) and (7);

(2) we calculate CIVG as a starting model using Eq. (6) with the effective equivalent storage (Eq. (11)) and subdomain techniques (Eq. (14)) for fast computation;

(3) we use the steepest descent method for iteration inversion, containing the effective equivalent storage and subdomain techniques for increasing the computation speed;

(4) the final 3D density distribution is obtained after achieving the minimum error or the number of iterations by the steepest descent inversion method;

(5) output the results.

3. Synthetic Model Test

In this section, we apply our fast inversion strategy on two sets of synthetic data: 1) a prism model, and 2) an interface model. The computational time and root-mean-square error (RMSE) of each modeling and inversion are calculated by a personal computer with 4 GB RAM, 3.10 GHz processor on a 32-bit operating system. No priori geologic information has been used to constrain the inversions for either of the two data sets. Therefore, the density variance is from zero to infinity.

The first model (Model 1) consists of two close prismatic sources (solid lines) with same size. They are buried at a depth of 5 km with a density contrast of 0.1 g/cm^3. The 3D domain is divided into $50\times 50\times 20$ cubic prisms with a grid spacing of 1 km. We add pseudo-random Gaussian noise to the synthetic data with mean value of zero and standard deviation of 0.03 mGal. The gravity anomaly is calculated on a 50×50 km^2 grid with a grid spacing of 1 km along the x- and y-directions (Figure 3a).

Figure 3b shows the anomaly calculated by taking a semi-infinite model with density contrast of 0 g/cm^3. This is usually used as starting values of density in the inversion when there is no prior information available. Figure 3d and g shows the estimated density distribution after 10 iterations at slices of $z = 1$ km and $y = 25$ km,

DOI: https://doi.org/10.30564/jgr.v1i2.845

respectively. The calculated gravity perfectly matches the observed values with an RMSE of 0.12. The density distributions are mainly concentrated in a shallow subsurface with very small density values. Figure 3c shows the estimated anomaly using our inversion strategy by taking CIVG as a starting model, while Figure 3e and h shows the density distribution of the starting model, and Figure 3f and i show the inverted results after 15 iterations at slices of $z = 1$ km and $y = 25$ km, respectively. It can be seen that the CIVG produces smooth models (Figure 3e and h). The final density distribution generates a clear, sharp, high-quality image, and the density value is close to the actual value (Figure 3f and i).

To further evaluate the computational efficiency of our inversion strategy, we use a more complex basement interface model (Model 2) with a density contrast of 0.2 g/cm^3 (Figure 4). The 3D domain is divided into $150 \times 30 \times 10$ cubic prisms with a grid spacing of 1 km along the x -, y - and z -directions. Figure 4a presents the synthetic gravity anomaly and Figure 4b shows the starting model using CIVG at slice of $y = 15$ km. Figure 4c and d shows the estimated anomaly and the inverted result at slice of $y = 15$ km without the subdomain technique. Figure 4e and f shows the estimated anomaly and the inverted result with subdomain technique. The observation anomaly can be fitted using the proposed procedure in this study with or without subdomain technique from comparing Figure 4c and e with Figure 4a. Meanwhile, comparing with Figure 4b, the result of our method (Figure 4d and f) clearly outlines the fluctuation of the interface and enhances the visibility and sharpness of geological structures, and is close to the true interface.

Table 1 shows the statistical information of the two different synthetic models. Form Model 1, although the semi-infinite model can reconstruct the anomaly with fewer iterations, less time than CIVG, the density distribution is quite deviate from the true position and the numerical value is smaller than the actual value. It is worth noting that the small RMSE and good fitting of anomaly do not represent the real underground density distribution, which is the manifestation of multi-solution inversion. Therefore, CIVG is a better choice as a starting model without prior information. Form Model 2, Subdomain technique takes less time and has smaller RMSE with the same number of iterations, comparing between Figure 4d and f. Subdomain technique greatly improves computational efficiency without losing accuracy, the larger the data set, the more efficient our method. It should be pointed out that we can reduce the grid spacing to achieve higher resolution results with the time and memory decreasing by our method.

4. 3D Gravity Inversion of the Northern Sinai Peninsula

In this section, we further apply our 3D inversion method to obtain density distributions of the Northern Sinai Peninsula and compare our density results with previous study [11]. The Sinai Peninsula is located between the Mediterranean and Red seas and is bounded by the Gulf of Suez to the west and the Dead Sea Transform to the east (Figure 5). The study area is a continental block between the African and Arabian plates, and underwent complex tectonics due to the interactions of different tectonic units. During the Late Triassic, the breakup of the north Afro-Arabian plate and the opening of the Tethys reactivated ENE-WSW trending deep faults. As the African plate moved towards to the Eurasian plate, the Tethys Sea began to close during the Late Cretaceous to pre-Miocene times, resulting in a series of NE-ENE oriented doubly plunging folds originated from inversion of the Mesozoic extensional basins in the Northern Sinai Peninsula. These inversion folds connected with the Syrian Arc Fold Belt to the northeast [12,21]. The aim of the present study is to carry out 3D gravity inversion to obtain density distribution of the Northern Sinai Peninsula and to help further understand the major tectonic and geologic characteristics.

The Bouguer gravity anomaly is reproduced in Figure5a after digitizing the anomaly presented by Khalil et al.[11]. A gravity high is observed at Risan Aniza to the south of EI-Arish, and it decreases gradually to a medium value at Sheikh Zwayed, whereas gravity lows are observed to the southeast of Risan Aniza. Figure 6b shows the residual anomalies based on the method of Abdelrahman et al. [1]. Both Risan Aniza and Sheikh Zwayed show high positive values on the residual Bouguer anomaly map, indicating high density bodies underneath these regions. Southeast of Risan Aniza, large area exhibits negative anomalies, implying low densities at depth. In this study, we utilize the inversion strategy proposed in section 2.5 to obtain the 3D density distributions from the residual Bouguer anomalies (Figure 6b).

The inversion domain is divided into $101 \times 113 \times 10$ cubic prisms with a grid spacing of 1 km along the x -, y - and z -directions. The background density value is taken as 2.67 g/cm^3, and the minimum and maximum density values are assumed to be 2.2 g/cm^3 and 2.9 g/cm^3 according to the known geological and geophysical investigations of the study area, respectively. Therefore, the density contrast ranges from -0.47 to 0.23 g/cm^3 across the study area.

 DOI: https://doi.org/10.30564/jgr.v1i2.845

Figure 7 shows the initial density distributions, which are calculated by the linear superposition of relative densities (calculated from correlation images based on Eq. (6)) and the background density (2.67g/cm^3) at different depths (1, 2, 3, 5, 10 and 20 km). Figure7a shows the estimated gravity anomaly after 12 iterations, and the computational time and RMSE are 21 s and 0.19, respectively. The fitting errors, which are the differences between the residual and estimated data, are shown in Figure 8b.

Figure 9 shows the final density distributions at the corresponding depths. Although the final density maps are very similar with the initial density images (Figure 7), there are big differences in the values of density. Our final density distribution model shows distinct high values beneath Risan Aniza at all depth slices (Figure 9). High density bodies are also observed under Sheikh Zwayed at depths between 3 and 20 km. It is interesting that the region to the southeast of Risan Aniza exhibits a slight high density anomaly below 5 km and an evident low density anomaly between 10 and 20 km. Li et al. [13] presented relatively small Curie depths in the same region, indicating a thermal anomaly at depth, therefore resulting in low density bodies to the southeast of Risan Aniza. Based on the horizontal slices, we suggest that there are two deep regional NE-SW trending faults around the high-density contrasts in the northern and southern edges of the Risan Aniza fold zone. We also build a density profile AA1 across EI Arish and Risan Aniza (Figure 9g), which shows medium and high density bodies beneath these two regions, respectively. To the southeast of Risan Aniza, the density distribution changes distinctly from low to high anomalies at depth, which may be caused by hot materials in the lower crust.

5. Conclusions

In this paper, we present a 3D gravity inversion method based on correlation image to recover density distributions in space domain. Our method applies CIVG as a starting model to generate a higher resolution image. In addition to the effective equivalent storage, we propose the subdomain techniques for fast calculation of the forward modeling and correlation image, which can reduce the consumption of memory without losing accuracy. We verify the feasibility and stability of our method by testing on both the synthetic and field data. High densities are observed beneath Risan Aniza, whereas low densities exist to the southeast of Risan Aniza at depths between 10 and 20 km, which may be resulted from hot anomalies in the lower crust.

Acknowledgements

We would like to thank the Editor Professor Sayed Hemeda and an anonymous reviewer for their insightful and constructive reviews and comments. This research is funded by the Institute of Crustal Dynamics, China Earthquake Administration (Grant No. ZDJ2019-09), the National Science Foundation of China (Grant No. 41704086), and the National Key Research & Development Program (2016YFC060110401).

Supplements

Table 1. Statistical information of two different synthetic models

Model	Starting model	Subdomain technique	Iterations	RMSE	Computation time(s)
Model 1	Semi-infinite	NO	10	0.12	22
Model 1	CIVG*	NO	15	0.12	44
Model 2	CIVG	NO	16	0.45	63
Model 2	CIVG	YES	16	0.32	46

Note: *CIVG is 3D correlation image of the vertical gradient of gravity data.

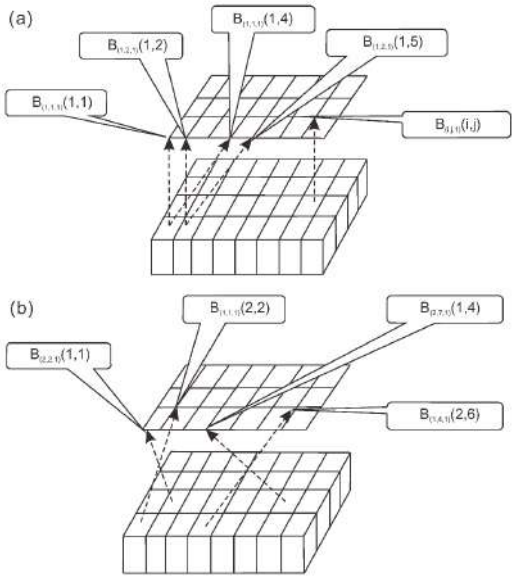

Figure 1. Illustration of the equivalent storage technique

Note: (a) equivalence of shift, and (b) symmetry reciprocation. $B_{(i,j,1)}(i,j)$ is the geometrical function of Eq. (2), the subscript $(i,j,1)$ is the source point, and (i,j) is the observation point at sea level.

DOI: https://doi.org/10.30564/jgr.v1i2.845

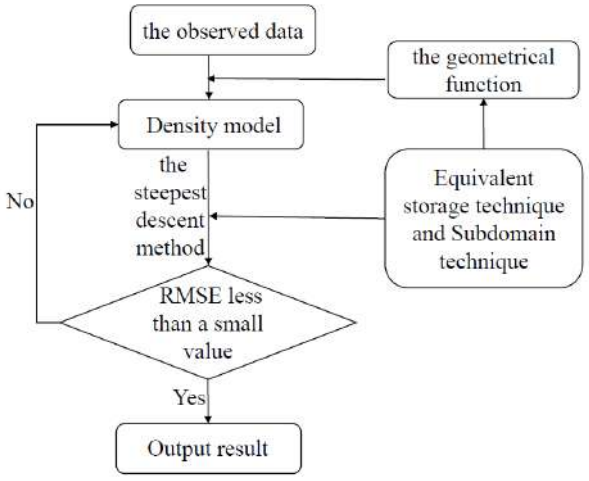

Figure 2. Flow chart of 3D gravity inversion with CIVG in space domain

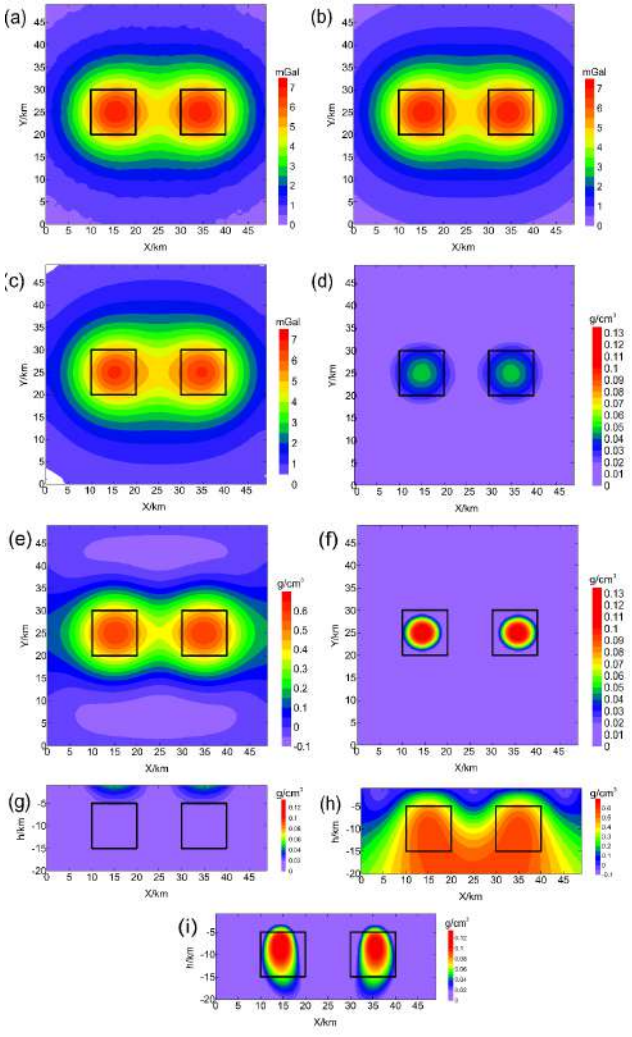

Figure 3. Synthetic tests on the prism model

Note: (a) theoretical gravity anomaly, (b) gravity anomaly calculated by taking the density contrast as 0 g/cm^3 based on a semi-infinite model, (c) estimated gravity anomaly based on our inversion strategy with CIVG, (d) estimated density distribution from the semi-infinite model with density contrast of 0 g/cm^3 at slice of z=1 km, (e) density distribution of starting model at slice of z=10 km, (f) inverted result at slice of z=10 km, (g) estimated density distribution from the semi-infinite model at slice of y=25 km, (h) density distribution of the starting model at slice of y=25 km, and (i) inverted result at slice of y=25 km. The black lines are the boundaries of the synthetic models.

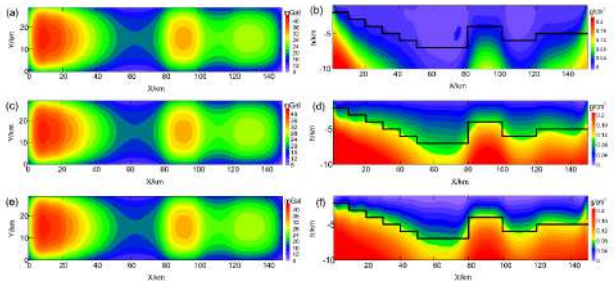

Figure 4. Synthetic tests on the interface model

Note: (a) theoretical gravity anomaly, (b) the starting model using CIVG at slice of y=15 km, (c) estimated gravity anomaly without subdomain technique, (d) inverted result without subdomain technique at slice of y=15 km, (e) estimated gravity anomaly with subdomain technique, and (f) inverted result with subdomain technique at slice of y=15 km. The black lines are the boundaries of the synthetic models.

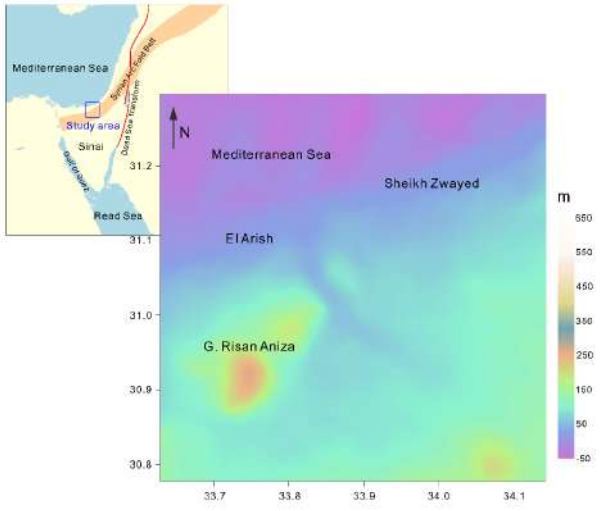

Figure 5. Topographic map of the study area. The inset shows the regional tectonic map of the Sinai and the neighboring area

DOI: https://doi.org/10.30564/jgr.v1i2.845

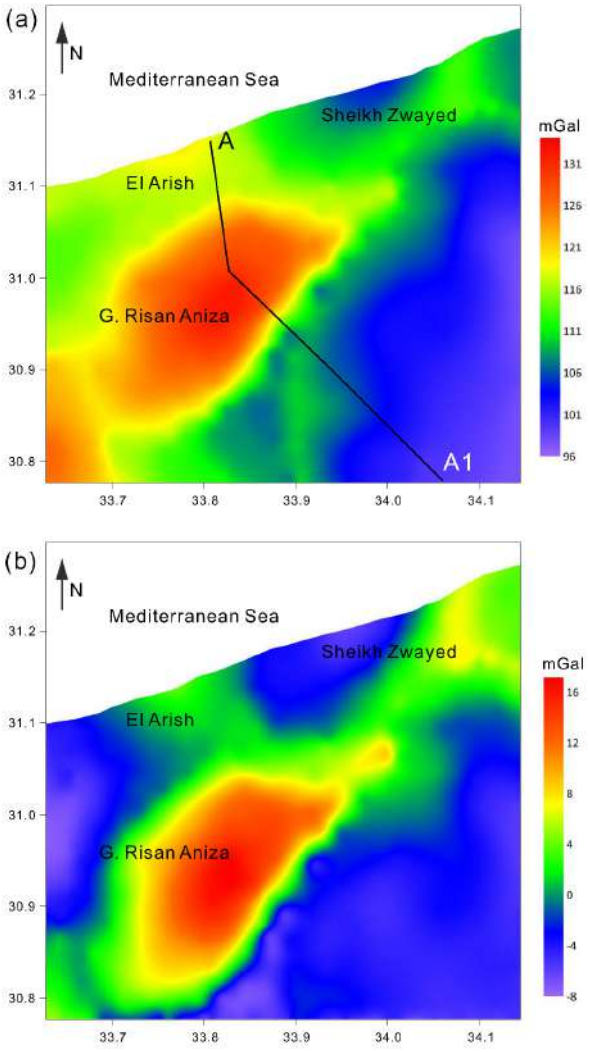

Figure 6. (a) Digitized Bouguer gravity anomaly of the Northern Sinai Peninsula [11]. The black line is the location of density profile AA1 for Figure 9g. (b) Residual Bouguer gravity anomaly of the Northern Sinai Peninsula

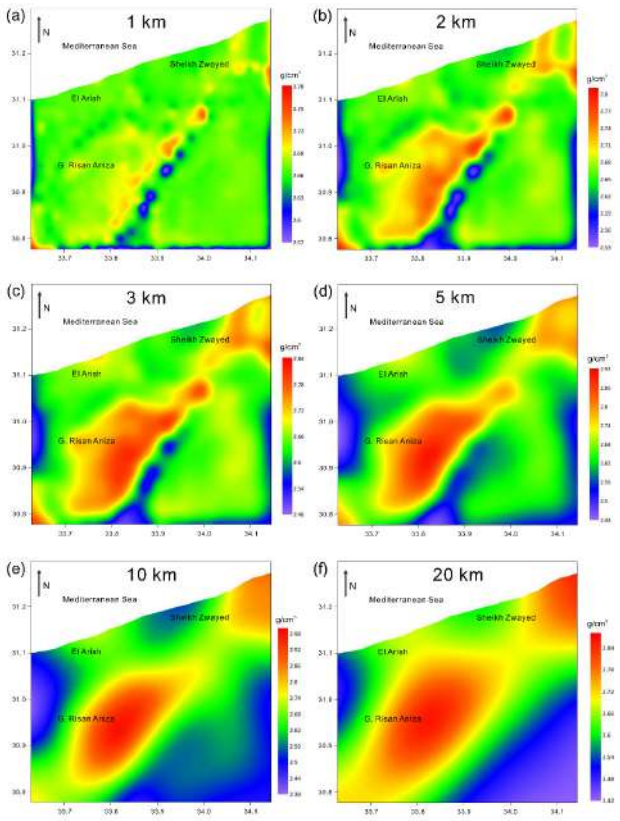

Figure 7. Initial density models at different depths of (a) 1km, (b) 2 km, (c) 3 km, (d) 5 km, (e) 10 km and (f) 20 km

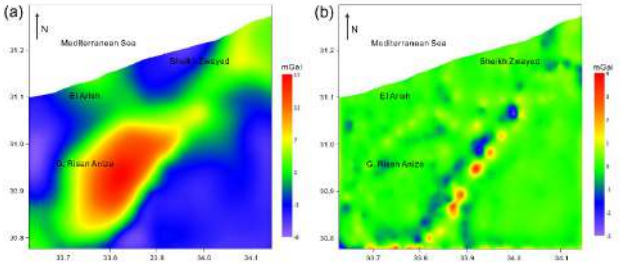

Figure 8. (a) Estimated gravity anomaly after 12 iterations and (b) differences between the residual and estimated gravity data

DOI: https://doi.org/10.30564/jgr.v1i2.845

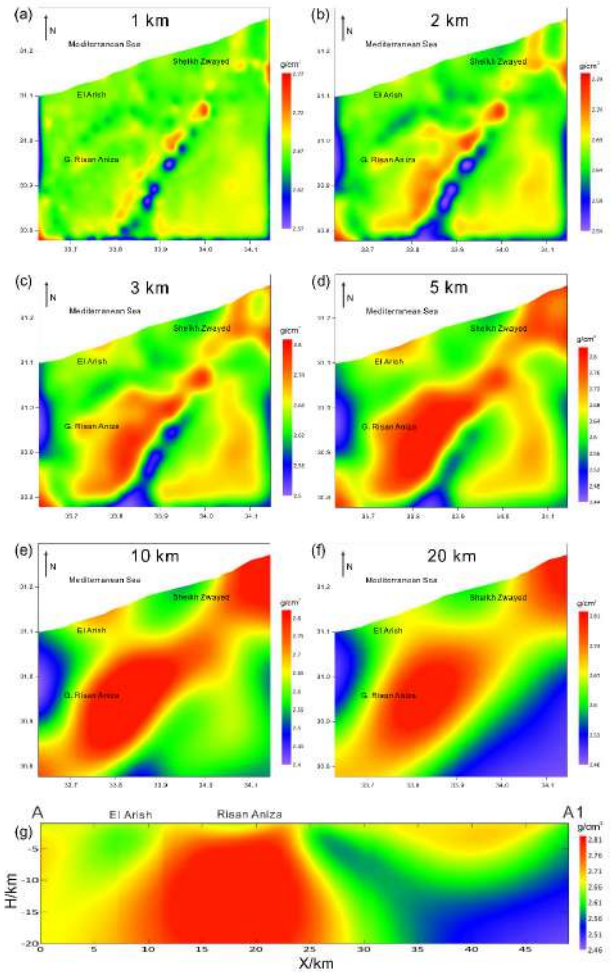

Figure 9. Estimated density distributions at different depths of (a) 1 km, (b) 2 km, (c) 3 km, (d) 5 km and (e) 10 km and (f) 20 km, and (g) is the density distribution profile AA1 according to Figure 6a

References

[1] Abdelrahman, E.M., Radwan, A.H., Issawy, E.A., El-Araby, H.M., El-Araby, T.M., Abo-Ezz, E.R.. Gravity interpretation of vertical faults using correlation factors between successive least-squares residual anomalies. Mining Pribram Symp. on Mathematical Methods in Geology, 1999, MC2: 1-6.

[2] Abedi, M., Gholami, A., Norouzi, G.H., Fathianpour, N.. Fast inversion of magnetic data using Lanczos bidiagonalization method. Journal of Applied Geophysics, 2013, 90: 126-137.

[3] Baniamerian J., Oskooi B. and Fedi M.. ource imaging of potential fields through a matrix space-domain algorithm, Journal of Applied Geophysics, 2017, 136: 51.

[4] Baniamerian J., Fedi M. and Oskooi B.. Compact Depth from Extreme Points: a tool for fast potential field imaging. Geophysical prospecting, 2016, 64: 1386-1398.

[5] Charles F. Van Loan.. Computational Frameworks for the Fast Fourier Transform, 1992.

[6] Chauhan M.S., Fedi M. and Mrinal K. S..Gravity inversion by the Multi-Homogeneity Depth Estimation method for investigating salt domes and complex sources, Geophysical Prospecting, 2018, 66: 175-191.

[7] Fedi M.. "DEXP: A fast method to determine the depth and the structural index of potential fields sources." Geophysics, 2007, 72(1): I1-I11.

[8] Fedi M. and Pilkington M.. "Understanding imaging methods for potential field data." Geophysics, 2012, 77(1): G13-G24.

[9] Gibert D. and Sailhac P.. Comment on: self-potential signals associated with preferential grounwater flow pathways in sinkholes. Journal of Geophysical Research, 2008, 113.

[10] Guo, L.H., Meng, X.H., Shi, L.. 3D correlation imagingof the vertical gradient of gravity data. J Geophys Eng, 2011, 8: 6-12.

[11] Khalil, M.A., Santos, F.M.. 3D Gravity Inversion of Northern Sinai Peninsula: A Case Study. Pure Appl Geophys, 2014, 171: 1557-1569.

[12] Khalil, M.A., Santos, F.M., Farzamian,M.. 3D gravity inversion and Euler deconvolution to delineate the hydro-tectonic regime in El-Arish area, northern Sinai Peninsula. Journal of Applied Geophysics,2014, 103: 104-113.

[13] Li, C.-F., Lu, Y. and Wang, J.. A global reference model of Curie-point depths based on EMAG2. Scientific Reports, 2017, 7: 45129.

[14] Li, Y., Oldenburg, D.W.. 3-D inversion of magnetic data. Geophysics, 1996, 61: 394-408.

[15] Li, Y., Oldenburg, D.W.. 3-D inversion of gravity data. Geophysics, 1998, 63: 109-119.

[16] Li, Y.G., Oldenburg, D.W.. Fast inversion of large-scale magnetic data using wavelet transforms and a logarithmic barrier method. Geophys J Int, 2003, 152: 251-265.

[17] Liu, G., Yan, H., Meng, X., Chen, Z. An extension of gravity probability tomography imaging. Journal of Applied Geophysics, 2014, 102: 62-67.

[18] MohammadRezaie, AliMoradzadeh and Ali NejatiKalateh, Fast 3D inversion of gravity data using solution space priorconditioned lanczos bidiagonalization, Journal of Applied Geophysics,2017, 136: 42-50.

[19] Mauriello, P., Patella, D.. Gravity probability tomography: a new tool for buried mass distribution imaging. Geophysical Prospecting, 2001, 49: 1-12.

 DOI: https://doi.org/10.30564/jgr.v1i2.845

[20] Meng, X.H., Liu, G.F., Chen, Z.X., Guo, L.H.. 3-D gravity and magnetic inversion for physical properties based on residual anomaly correlation (in Chinese with English abstract). Chinese Journal of Geophysics, 2012, 55: 304-309.

[21] Moustafa A.R.. Structural setting and tectonic evolution of North Sinai folds, Egypt. In Homberg, G. and Bachmann, M. (eds). Evolution of the Levant Margin and Western Arabia Platform since the Mesozoic. Geological Society, London, Special Publications, 2015, 341: 37-63.

[22] Patella, D.. Introduction to ground surface self-potential tomography. Geophysical Prospecting, 1997, 45: 653-681.

[23] Portniaguine, O., Zhdanov, M.S.. Focusing geophysical inversion images. Geophysics, 1999, 64: 874-887; 3-D magnetic inversion with data compression and image focusing. Geophysics, 2002, 67: 1532-1541.

[24] Shamsipour, P., Chouteau, M., Marcotte, D.. 3D stochastic inversion of magnetic data. Journal of Applied Geophysics, 2011, 73: 336-347.

[25] Shamsipour, P., Marcotte, D., Chouteau, M., Keating, P.. 3D stochastic inversion of gravity data using cokriging and cosimulation. Geophysics, 2010, 75: I1-I10.

[26] Tikhonov, A.N., Arsenin, V.Y.. Solution of ill-posed Problems. Winston, 1977.

[27] Yao, C.L.. High speed computation and efficient storage in 3D gravity and magnetic inversion based on genetic algorithms (in Chinese with English abstract). Cheinese Journal of Geophysics, 2003, 46: 252-258.

[28] Yao, C.L., Zheng, Y.M., Zhang, Y.W.. 3-D gravity and magnetic inversion for physical properties using stochastic subspaces (in Chinese with English abstract). Cheinese Journal of Geophysics, 2007, 50: 1576-1583.

[29] Zhdanov, M.S.. Tutorial: Regularization in inversion theory. Center for Wave Phenomena, 1993: 1-47.

[30] Zhdanov, M.S.. Geophysical inverse theory and regularization problems. Elsevier, 2002.

[31] Zhao,G,D, Chen B., Chen L.W, Liu J.X, Ren Z.Y.. High-accuracy 3D Fourier forward modeling of gravity field based on the Gauss-FFT technique. Journal of Applied Geophysics, 2018, 150: 294-303.

DOI: https://doi.org/10.30564/jgr.v1i2.845

BILINGUAL PUBLISHING CO.
Pioneer of Global Academics Since 1984

Journal of Geological Research
https://ojs.bilpublishing.com/index.php/jgr-a

REVIEW

Review of Proposed Stress-dilatancy Relationships and Plastic Potential Functions for Uncemented and Cemented Sands

Mojtaba Rahimi*

Department of Mechanical Engineering, Khomeinishahr Branch, Islamic Azad University, Khomeinishahr/Isfahan, Iran

ARTICLE INFO

Article history
Received: 24 May 2019
Accepted: 26 September 2019
Published Online: 30 September 2019

Keywords:
Stress-dilatancy
Plastic potential function
Flow rule
Dilatancy rate
Plasticity
Sand
Cemented sand

ABSTRACT

Stress-dilatancy relationship or plastic potential function are crucial components of every elastoplastic constitutive model developed for sand or cemented sand. This is because the associated flow rule usually does not produce acceptable outcomes for sand or cemented sand. Many formulas have been introduced based on the experimental observations in conventional and advanced plasticity models in order to capture ratio of plastic volumetric strain increment to plastic deviatoric strain increment (i.e. dilatancy rate). Lack of an article that gathers these formulas is clear in the literature. Thus, this paper is an attempt to summarize plastic potentials and specially stress-dilatancy relations so far proposed for constitutive modelling of cohesionless and cemented sands. Stress-dilatancy relation is usually not the same under compression and extension conditions. Furthermore, it may also be different under loading and unloading conditions. Therefore, the focus in this paper mainly places on the proposed stress-dilatancy relations for compressive monotonic loading. Moreover because plastic potential function can be calculated by integration of stress-dilatancy relationship, more weight is allocated to stress-dilatancy relationship in this research.

1. Introduction

Variations of soil and rock volume may be caused by changes in the stress and deformation (mechanical effects) and changes in the water content, the temperature and other reasons (non-mechanical effects) [54]. The tendency of soil or rock to change volume while shearing is called dilatancy [18]. Dilatancy of sand and cemented sand is a crucial phenomenon which differentiates their plastic response from that of metal. That is, dilatancy is one of features of sand and cemented sand that can not be simulated appropriately by the traditional plasticity developed initially for metals. Usefulness of any elastoplastic constitutive model of sand or cemented sand may highly depends on successful implementation of dilatancy response. It is clear that loose sands or weakly cemented sands tend to develop positive pore pressure under undrained shear or to decrease volume under drained shear conditions. Conversely, dense sands and cemented sands tend to develop negative pore pressure in the course of shear or to increase in volume under drained shear conditions [7]. That is, dense sands dilate as deviator stress increases until failure while loose sands decreases in volume with progress of shear loading until failure. This is why dilatancy theory is normally discussed in the context of dense sands. However there is

**Corresponding Author:*
Mojtaba Rahimi,
Department of Mechanical Engineering, Khomeinishahr Branch, Islamic Azad University, Khomeinishahr/Isfahan, Iran;
Email: rahimi2726@gmail.com; rahimi@iaukhsh.ac.ir

 DOI: https://doi.org/10.30564/jgr.v1i2.864

usually nothing in proposed stress-dilatancy relations that limit their application to dense sands [4].

Note that in loose sands or weakly cemented sands, zero dilatancy takes places at large strains, but in dense sands, it happens twice during shearing: once temporary at phase transformation when response changes from contractive to dilative, and once at large strains when shearing continues at constant volume [16, 30].

The geotechnical literature uses the terms dilation and dilatancy interchangeably as we did in the last paragraphs. They are usually stated as an angle compared to friction angle. However, we can divide these two dilatancy definitions into two categories: 1) absolute definition: dilation is the volumetric strain change occurred since the initial condition 2) rate definition: dilation is the ratio of volume change increment relative to shear strain increment [18]. We use the rate definition of dilation in next sections.

Note that the stress-dilatancy equations and plastic potential functions are used extensively in this article. The plastic potential defines the direction of plastic strain increments. The plastic potential is usually expressed using a stress-dilatancy equation which relates the dilatancy rate to the stress ratio [21].

2. Background

According to the classical plasticity, there exist a plastic potential function such that normal to the function shows components of plastic strain increment. This is to say [12, 67, 68]:

$$\dot{\varepsilon}_{ij}^{p} = \lambda \frac{\partial g}{\partial \sigma_{ij}} \tag{1}$$

where $\dot{\varepsilon}_{ij}^{p}$ is plastic strain increment tensor, g is plastic potential function, σ_{ij} is stress tensor and λ is plasticity multiplier which is calculated using consistency condition.

This rule is called flow rule. Flow rule implies that the derivative of the plastic potential function is important in constitutive modelling rather than the function itself.

Stress-dilatancy relationship in triaxial space also is usually expressed as follows [4,9,35]:

$$d = \frac{\dot{\varepsilon}_{P}^{p}}{\dot{\varepsilon}_{q}^{p}} = \frac{\dfrac{\partial g}{\partial p'}}{\dfrac{\partial g}{\partial q}} \tag{2}$$

where d is the dilatancy rate, $\dot{\varepsilon}_{p}^{p}$ and $\dot{\varepsilon}_{q}^{p}$ are volumetric and deviatoric plastic strain increments accordingly, p' and q are mean effective stress and deviator stress, respectively.

Analysis of direct shear box test of sand by Taylor [57] implies that input work is entirely dissipated in friction. Therefore, we can equal plastic input work to the dissipated energy in friction for triaxial conditions as follows [6,7,34]:

$$\begin{aligned} p'\dot{\varepsilon}_{P}^{p} + q\dot{\varepsilon}_{q}^{p} &= Mp'\dot{\varepsilon}_{q}^{p} && \text{for triaxial compression} \\ p'\dot{\varepsilon}_{P}^{p} + q\dot{\varepsilon}_{q}^{p} &= -Mp'\dot{\varepsilon}_{q}^{p} && \text{for triaxial extension} \end{aligned} \tag{3}$$

M denotes the slope of critical state line in $p' - q$ space.

Arrangement of equation (3) gives rise to a very fundamental form of dilatancy equation as follows [6,19,34]:

$$d = \frac{\dot{\varepsilon}_{P}^{p}}{\dot{\varepsilon}_{q}^{p}} = \begin{cases} M - \eta & for\ compression \\ -M - \eta & for\ extension \end{cases} \tag{4}$$

η is stress ratio which is defined as q/p'.

Different values of M are used for triaxial compression and triaxial extension as follows:

$$M = \begin{cases} \dfrac{6\sin\phi_{cv}}{3 - sin\phi_{cv}} & for\ compression \\ \dfrac{6\sin\phi_{cv}}{3 + sin\phi_{cv}} & for\ extension \end{cases} \tag{5}$$

ϕ_{cv} is the constant volume (critical state) fiction angle.

From the above equation, it can be realized that M (the critical state stress ratio) for compression is greater than M for extension if the critical state friction angle is the same for both compression and extension.

In order to arrive in better match for experimental observations, a constant A is often introduced in equation (4) in the following form [15,16,69]:

$$d = \frac{\dot{\varepsilon}_{P}^{p}}{\dot{\varepsilon}_{q}^{p}} = A(M - \eta) \tag{6}$$

A is a material parameter which may be different for triaxial compression and extension loading and η is current stress ratio. A should be determined by curve fitting of equation (6) against total volume change [15,16].

Equation (4) can also be written in the form of equation (7) as follows [7]:

$$d = \frac{\dot{\varepsilon}_{P}^{p}}{\dot{\varepsilon}_{q}^{p}} = (M - \beta\eta) \tag{7}$$

β is a constant.

DOI: https://doi.org/10.30564/jgr.v1i2.864

Rowe [47] derived the stress-dilatancy relation for soils using minimum energy consideration for particle sliding as follows [4,41]:

$$\frac{\sigma_1^{'}}{\sigma_3^{'}} = K\left(1 - \frac{\dot{\varepsilon}_V}{\dot{\varepsilon}_1}\right) \quad for\ compression \tag{8}$$

$$\frac{\sigma_1^{'}}{\sigma_3^{'}} = \frac{K}{\left(1 - \frac{\dot{\varepsilon}_V}{\dot{\varepsilon}_1}\right)} \quad for\ extension \tag{9}$$

where K is a parameter which depends on the failure friction angle.

With presuming a constant failure friction angle and neglecting elastic strains, Wood [66] formulated Rowe's stress-dilatancy relation as follows [15, 62, 41]:

$$\begin{cases} d = \frac{\dot{\varepsilon}_p^p}{\dot{\varepsilon}_q^p} = \frac{9(M_c - \eta)}{9 + 3M_c - 2M_c\eta} & for\ compression \\ d = \frac{\dot{\varepsilon}_p^p}{\dot{\varepsilon}_q^p} = \frac{9(M_e - \eta)}{9 - 3M_e - 2M_e\eta} & for\ extension \end{cases} \tag{10}$$

where M_c and M_e are critical state stress ratio in triaxial compression and extension, respectively.

In addition to the constant critical state stress ratio, the variable phase transformation stress ratio (i.e. M_{PT}) [for example see 16, 42,43] and the failure stress ratio (i.e. M_f) have been used in equations (4), (6) and (10) as well. M_{PT} is a value corresponding to a temporary zero dilatancy which is calculated similar to equation (5) with replacement of the critical state friction angle by the phase transformation friction angle [6,69]. M_f also is not constant and evolves towards the critical state stress ratio with plastic shearing [4,16]. Replacement of the critical state stress ratio with M_{PT} or M_f is performed in order to account for the effect of pressure and density dependency of the stress-dilatancy relationship of sands [15].

3. Stress-dilatancy Relationships and Plastic Potential Functions

3.1 Cohesionless Sands

Proposed stress-dilatancy relationships and plastic potential functions are presented in a historical sequence. Most of formulas which are presented here are stress-dilatancy relationships. However, some proposed constitutive models have used a plastic potential function to define the direction of plastic flow as well. A summary of these stress-dilatancy relationships and plastic potential functions of uncemented sands with striking highlights is given in table 3 (see appendix section).

(1) Nova and Wood [35]:

Nova and Wood [35] used the following equation as their stress-dilatancy relationship:

$$d = \frac{M - \eta}{\mu} \tag{11}$$

where M and μ are positive constants and d is the dilatancy rate. At critical state, $\eta=M$ and hence dilatancy rate becomes zero which implies no volume change at the critical state. ($-1/\mu$) is the slope of the linear relation between $\dot{\varepsilon}_P^p/\dot{\varepsilon}_q^p$ and η.

Cui and Delage [8] applied the same equation as above in their constitutive model.

Plastic potential function associated with this stress-dilatancy relationship is as follows:

$$g(p^{'},q) = q - \frac{Mp^{'}}{1-\mu}\left[1 - \mu\left(\frac{p^{'}}{p_{ug}^{'}}\right)^{(1-\mu)/\mu}\right] \tag{12}$$

where $p_{ug}^{'}$ is value of the isotropic pressure when $\eta=M$. Note that when $\mu=1$, the equation reduces to that of the Cam Clay model.

(2) Nova and Wood [36]:

One of the oldest and most popular stress-dilatancy relationships proposed for cohesionless sands was first suggested by Nova and Wood [36]. It was formulated as follows:

$$d = (1 + \alpha_g)(M - \eta) \tag{13}$$

where $\eta=q/p^{'}$ is stress ratio, M is the critical state stress ratio and a_g is a material parameter.

Similar stress-dilatancy relationships were used by Pastor et al. [37], Haeri and Hamidi [13], Hamidi and Yarbakhti [14] and Kong et al. [25].

The above relationship results in the following plastic potential function:

$$g(p^{'},q) = q - Mp^{'}\left(1 + \frac{1}{\alpha_g}\right)\left[1 - \left(\frac{p^{'}}{p_g^{'}}\right)^{\alpha_g}\right] \tag{14}$$

where $p_g^{'}$ is a size parameter which determines size of the plastic potential function.

(3) Jefferies [17]:

Jefferies [17] used the below relationship in his critical state constitutive model to represent the stress-dilatancy behavior. It appears that the formula was proposed based on Nova and Wood [35]'s relation as follows:

DOI: https://doi.org/10.30564/jgr.v1i2.864

$$d = \frac{M - \eta}{1 - N} \tag{15}$$

where N is a material parameter and d is the dilatancy rate which is defined as plastic volumetric strain increment to plastic deviatoric strain increment.

If N=0 then the above equation reduces to the familiar Cam Clay model. Note that Andrade [2] used the same flow rule in his constitutive model.

Jefferies obtained the plastic potential function by integration of his stress-dilatancy relationship and then considered the yield function equals to the plastic potential function (associated flow rule).

Jefferies stated that their stress-dilatancy relationship and constitutive model in general capture the influence of void ratio and mean effective stress on sand response but neglect the influence of fabric (i.e. grain contact arrangement or geometrical packing of particles). He also claimed that the bedding direction during sample preparation pronouncedly affects stress-dilatancy relationship.

Jefferies suggested in his model that an infinite number of isotropic consolidation lines exist for sands which prevents the direct coupling of the yield surface size to the void ratio. This was a novelty in his model which resulted in change of focus from the normally consolidation line to the critical state line in definition of the hardening law. That is, he applied a shear hardening law instead of a volumetric hardening law.

(4) Lagioia et al. [27]:

Lagioia et al. [27] proposed their stress-dilatancy relationship such that the proposed formula fulfills the two following requisites:

$$\begin{cases} \eta \to 0 \implies d \to \infty \\ \eta = M \implies d = 0 \end{cases} \tag{16}$$

This implies that when a material is sheared isotropically (η=0), only plastic volumetric strain occurs and also when the stress ratio reaches the critical state value of M in compressive loading, the critical state condition must meet [27]. The following stress-dilatanccy relation satisfies the two aforementioned conditions:

$$d = \mu_g (M - \eta)\left(\frac{\alpha M}{\eta} + 1\right) \tag{17}$$

α and μ_g are model constants. η is the current stress ratio and M is critical state stress ratio which is deifned based on equation (5).

Similar to Jefferies [17], Lagioia et al. [27] integrated the above equation and considered it equals to the yield function (associated flow rule).

Note that similar stress-dilatancy equation was later used by DeSimone and Tamagnini [9].

(5) Yu [71]:

Yu [71] used the well-known Rowe's stress-dilatancy relationship (equation (10)) in his proposed constitutive model named CASM to relate stress ratio and dilatancy rate. Yu [71] stated that despite immense effort to develop a better stress-dilatancy relation for sands compared to Rowe's original or modified relationship, little progress appears to have been made in this area. Based on Rowe's stress-dilatancy relation, Yu [71] and Yu et al. [72] obtained the following relation for the plastic potential of sands and clays:

$$g(p',q) = 3M\left(lnp' - ln\beta_g\right) + (3 + 2M)\ln\left(\frac{3p' + 2q}{p'}\right) - (3 - M)\ln\left(\frac{3p' - q}{p'}\right) \tag{18}$$

The size parameter β_g is a dummy parameter as only the derivative of the plastic potential function with respect to p' and q is important.

Note that the adopted stress-dilatancy relation in CASM is non-associated flow rule as the plastic potential function is not the same as the proposed yield function in this model.

(6) Schanz et al. [15]:

Schanz et al. [15] used the following equations as the flow rule:

$$sin\psi_m = \frac{sin\varphi_m - sin\varphi_{cv}}{1 - sin\varphi_m sin\varphi_{cv}} \tag{19}$$

where Ψ_m is the mobilized dilatancy angle, φ_m is the mobilized friction angle and φ_{cv} is the critical state friction angle which is a material constant. φ_m is calculated by below equation:

$$sin\varphi_m = \frac{\sigma_1' - \sigma_3'}{\sigma_1' + \sigma_3' - 2coh.cot\varphi_p} \tag{20}$$

where φ_p is the failure friction angle. This equation can easily be proved by shape of a Mohr-Coulomb failure envelope.

The above equations correspond to the famous Rowe's stress-dilatancy theory [15].

Note that the critical state dilation angle can be calculated by the failure friction and dilation angles as follows:

$$sin\psi_{cv} = \frac{sin\varphi_p - sin\psi_p}{1 - sin\varphi_p sin\psi_p} \tag{21}$$

DOI: https://doi.org/10.30564/jgr.v1i2.864

The above definition of the flow rule is equivalent to the definition of the plastic potential function in the form of below equation [15]:

$$g = \frac{\left(\sigma_1^{'} - \sigma_3^{'}\right)}{2} - \frac{\left(\sigma_1^{'} + \sigma_3^{'}\right)}{2} sin\psi_m \tag{22}$$

(7) Wan and Guo [61]:

Wan and Guo [61] presented a fabric dependent stress-dilatancy equation as follows:

$$d = \frac{-4}{3} \frac{(sin\varphi_m - sin\varphi_f)}{\left(1 - sin\varphi_f sin\varphi_m\right)} \tag{23}$$

Depending on magnitude of the characteristic friction angle (φ_f) relative to that of the mobilized friction angle (φ_m), the dilatancy rate changes its sign. This enables the model to capture the change in volumetric response from contractive to dilative which usually observed in dense sands experimentally.

The characteristic and mobilized friction angle in this model are defined as follows:

$$sin\varphi_f = \frac{X\left(\frac{F_{33}}{F_{11}}\right) + \gamma^{P^*}}{a + \gamma^{P^*}} \left(\frac{e}{e_{cr}}\right)^{\alpha} sin\varphi_{cv} \tag{24}$$

where F_{11} and F_{33} are fabric tensor components in the axial and radial directions, respectively.γ^{P^*} is the true shear strain. X, a and α are material constants. e is the current void ratio and e_{cr} is the critical state void ratio.

$$sin\varphi_m = \frac{\gamma^{P^*}}{a + \gamma^{P^*}} \left(\frac{e}{e_{cr}}\right)^{-\beta_1} sin\varphi_{cv} \tag{25}$$

where β_1 is a material parameter.

(8) McDowell [31]:

McDowell [31] proposed the following stress-dilatancy relation for sand in his constitutive model:

$$d = \frac{M^{b+1} - \eta^{b+1}}{\eta^b} \tag{26}$$

where d is dilatancy ratio, $\eta = q/p^{'}$ is current stress ratio and M is the critical state stress ratio and b is a material parameter.

The plastic potential associated with this stress-dilatancy equation is defined as follows:

$$g\left(p^{'}, q\right) = \eta - M\left[(b+1)\ln\left(\frac{p_p^{'}}{p^{'}}\right)\right]^{\frac{1}{b+1}} \tag{27}$$

$p_p^{'}$ is the value of $p^{'}$ at q=0

McDowell's stress dilatancy equation fulfills the necessary conditions of zero shear strain under isotropic conditions $(\eta = 0 \rightarrow \varepsilon_q^p = 0 \rightarrow d = \infty)$ and infinite shear strain with zero volumetric strain at the critical state . $(\eta = M \rightarrow \varepsilon_q^p = \infty \;\&\; \varepsilon_p^p = 0 \rightarrow d = 0)$ This approach is identical to that suggested by Lagioia et al. [27].

(9) Russell and Khalili [48]:

Russell and Kalili [48] used the following equation as the streee-dilatancy relation:

$$d = M_f - \eta = (1 + k_d \xi) - \eta \tag{28}$$

where k_d is a material paramter and ξ is the state parameter.

M_f is used in above equation instead of M to capture the dependency of d on density and confining pressure through k_d and ξ.

Russell and Kalili [48]'s model was developed in a critical state framework. Certain features of the model are linked to the state parameter (ξ), which is a dimensionless parameter defined as the vertical distance between the current state and the critical state line in the $e - p^{'}$ plane. The state parameter is positive on the loose (wet) side of the critical state line (CSL) and negative on the dense (dry) side of CSL, and expressed as:

$$\xi = e - e_{cs} \tag{29}$$

where e is the void ratio at the current stress state ($p^{'}$), and e_{cs} the void ratio at the critical state corresponding to $p^{'}$.

(10) Been and Jefferies [4]:

Been and Jefferies [4] summarized the existing stress-dilatancy relations according to the table 1 and table 2:

Table 1. Summary of stress-dilatancy relationships [4]

Theory	Relationship
Cam Clay	$d=M_f-\eta$
Modified Cam Clay	$d=(M^2_f-\eta^2)/2\eta$
Jefferies ([17]	$d=(M_f-\eta)/(1-N)$
Li and Dafalias [29]	$d=d_0(M_f-\eta)/M$
Rowe [47]	$d=9(M_f-\eta)/(9+3M_f-2M_f\eta)$

Table 2. Summary of proposed relationships for M_f[4]

Authors	Relationship	Comments
Manzari and Dafalias [33]	$M_f=M+m\xi$	ξ is the state parameter.

DOI: https://doi.org/10.30564/jgr.v1i2.864

Li and Dafalias [29]	$M_f=Mexp(m\xi)$	ξ is the state parameter.
Jefferies and Schuttle [19]	$M_f=M-\lvert\xi_i\rvert$	$\xi_i=\xi-\lambda(1-\eta/M)$
Wang et al. [64]	$M_f=M_0+(M-M_0)I_p$	$\xi=\lambda\ln(I_p)$

Note: λ is slope of the critical state line. m and M_0 are positive model constants.

(11) Dafalias and Manzari [33]:

Dafalias and Manzari [33] proposed their stress-dilatancy equation based on difference between the current stress ratio η and the dilatancy stress ratio M_{PT} which is known as the phase transformation stress ratio. The suggested relationship is as follow:

$$d = A_d(M_{PT} - \eta) \tag{30}$$

where A_d is material parameter.

For dense sands under small shear strains, $\eta < M_{PT}$ which leads to $d > 0$ (compressive behavior). However, with progress of loading, η becomes equal to M_{PT} at a point which results in d=0 (temporary steady state response). Further shearing leads to $\eta > M_{PT}$ which results in $d < 0$ (dilative behavior). Ultimately, the phase transformation stress ratio becomes equal to the current stress ratio at the critical state which leads to zero dilatancy rate (permanent steady state response). Note that the phase transformation state is never reached during shearing of loose sands and η is always smaller than M_{PT} leading to prediction of permanent contraction during shearing.

Dafalias and Manzari made A_d fabric dependent. To avoid lengthy discussion, fabric dependency of the stress-dilatancy relationship is not discussed here. Interested reader is referred to Dafalias and Manzari [33].

(12) Khalili et al. [23]:

The stress-dilatancy equation which was proposed by Khalili et al. [23] is similar to that of Russell and Khalili [48]. The proposed relation is as follows:

$$d = M_f - \eta = (1 + k_d\xi)M - \eta \tag{31}$$

where k_d is a material constant, ξ is the state parameter and M is the critical state stress ratio.

The variable M_f is used in place of the constant M to account for the dependency of d on void ratio (or density).

Integration of the above stress-dilatancy relation with respect to p' and q results in the following plastic potential function:

$$g(p', q, p_0) = q + (1 + k_d\xi)Mp'ln\frac{p'}{p_0} \tag{32}$$

As mentioned already ξ is a dimensionless parameter defined as the vertical distance between the current state and the critical state line in the v *vs.*$\ln p'$ plane. It is expressed as:

$$\xi = \nu - \nu_{cs} \tag{33}$$

where v=1+e is the specific volume at the current stress state (p'), e is the void ratio, and v_{cs} is the specific volume at the critical state corresponding to p'.

(13) Imam et al. [16]:

Imam et al. presented their stress-dilatancy relation based on concept of the phase transformation stress ratio M_{PT} as follows:

$$d = A(M_{PT} - \eta) \tag{34}$$

A is calculated for triaxial compression and triaxial extension, respectively, as follows:

$$\begin{cases} A_c = \dfrac{9}{9 + 3M_{PT,c} - 2M_{PT,c}\eta} \\ A_e = \dfrac{9}{9 - 3M_{PT,c} - 2M_{PT,c}\eta} \end{cases} \tag{35}$$

where

$$\begin{cases} M_{PT,c} = \dfrac{6sin\varphi_{PT,c}}{3 - sin\varphi_{PT,c}} \\ M_{PT,e} = \dfrac{6sin\varphi_{PT,e}}{3 + sin\varphi_{PT,e}} \end{cases} \tag{36}$$

and

$$\begin{cases} sin\varphi_{PT,c} = sin\varphi_{cs} + k_{PT}\xi \\ sin\varphi_{PT,e} = sin\varphi_{cs} + k_{PT}\xi + a_{PT} \end{cases} \tag{37}$$

where k_{PT} and a_{PT} are material parameters, φ_{cs} is the critical state friction angle, φ_{PT} is the phase transformation friction angle, M_{PT} is the phase transformation stress ratio and ξ is the state parameter.

The plastic potential function associated with the above flow rule is obtained by the following relationship:

$$g(p', q) = \eta - M_{PT}\left(\frac{A}{A-1}\right)\left[1 - \left(\frac{p'}{p'_0}\right)^{A-1}\right] \qquad for\ A \neq 1 \tag{38}$$

in which p'_0 is a measure of the size of the plastic potential function.

DOI: https://doi.org/10.30564/jgr.v1i2.864

The same stress-dilatancy equation was used by Tasiopoulou and Gerolymos [56] in their model. They, however, assigned a value of one for A.

(14) Ling and Yang [30]:

Ling and Yang [30] used a combination of work of Nova and Wood [36] and Li and Dafalias [29] to define their stress-dilatancy relation as follows:

$$d = (1 + \alpha_g)(M_f - \eta) \tag{39}$$

$$M_f = M \exp(m\xi) \tag{40}$$

where α_g and m are positive constants and ξ is the state parameter. α_g and m can be determined using the volumetric strain vs. deviator strain curve.

The difference between the above equation with that of Nova and Wood is that a variable stress ratio M_f (which changes with the void ratio and mean effective stress) has been used rather than the constant critical state stress ratio M.

The state parameter at the phase transformation for dense sands temporary becomes zero which enables the constitutive model to capture the phase transformation state. However for loose sands, the void ratio is always greater than the critical state void ratio which leads to a positive state parameter. The net result is that M_f is always greater than the current stress ratio which implies that the dilatancy rate is always positive for loose sands (i.e. permanent contractive behavior) except at the critical state in which the dilatancy rate becomes zero. This implies that no volume change occurs at the critical state neither for loose sands nor dense sands because at the critical state, the state parameter is zero which leads to $M_f=M=\eta$.

Liu et al. [32] considered the similar stress-dilatancy equation in their model. However, they replaced M_f with the phase transformation stress ratio.

(15) Sasiharan [49]:

Sasiharan [49] suggested the following stress-dilatancy equation in his anisotropic sand model:

$$d = \frac{M^2 + \alpha_g^2 - \eta^2}{2(\eta - \alpha_g)} \tag{41}$$

where is fabric anisotropy parameter which is defined according to the following formula:

$$\alpha_g = \left(\frac{e}{1+e}\right)\beta \tag{42}$$

in which e is current void ratio and β is a material parameter. Thus, the fabric anisotropy parameter evolves with the void ratio.

The plastic potential function corresponds to the above stress-dilatancy relationship is as follows:

$$g(p',q) = \frac{p'}{p'_{cg}} - \frac{M^2}{M^2 + (\eta - \alpha_g)^2} \tag{43}$$

where p'_{cg} is the value of p' when $\eta=a_g$.

Similar to Jefferies's approach and conventional Cam Clay model, Sasiharan considered the resulting plastic potential function, obtained by integration of the flow rule, identical to the yield function.

If the fabric anisotropy parameter a_g is zero, the yield and plastic potential surfaces will be an ellipse that is centered along the p' axis as in modified Cam Clay model.

Sasiharan [49] stated that the above stress-dilatancy relation is not appropriate for anisotropic sands and suggested the following flow rule instead:

$$d = \frac{M^2 - (\eta - \alpha_g)^2}{2(\eta - \alpha_g)} \tag{44}$$

$\eta = (M^2 + \alpha_g^2)^{\frac{1}{2}}$ for the first flow rule and $\eta = \pm M + \alpha_g$ for the second flow rule constitute the phase transformation line (i.e. zero dilatancy line) on which zero plastic strain increment occurs.

Note that similar stress-dilatancy relationships were mentioned in Muhunthan and Sasiharan [34].

(16) Tasiopoulou and Gerolymos [55]:

Tasiopoulou and Gerolymos [55] presented their stress-dilatancy equation as follows:

$$d = M_{PT} - \zeta M_s \tag{45}$$

where M_{PT} is the phase transformation stress ratio, M_S is ultimate strenght stress ratio in q-p' space, and ζ is the hardening parameter which evolves with shearing and is defined as:

$$\zeta = \left|\frac{q}{M_s p'}\right|^n \tag{46}$$

where n is an exponential parameter which controls the distance of the current stress state from the failure line.

The ζ parameter is bounded. Its values limit within the range of [-1,1]

(17) Kan et al. [21]:

Kan et al. [21] used the following plastic potential function:

DOI: https://doi.org/10.30564/jgr.v1i2.864

$$\begin{cases} g(p',q,\bar{\theta},p_0) = \tilde{t}q + \dfrac{AM(\bar{\theta})p'}{A-1}\left((\dfrac{p'}{p_0})^{A-1} - 1\right) & for\ A \neq 1 \\ g(p',q,\bar{\theta},p_0) = \tilde{t}q + M(\bar{\theta})\,p' \ln\left(\dfrac{p'}{p_0}\right) & for\ A = 1 \end{cases} \quad (47)$$

in which p_0 controls the size of the plastic potential surface, and A is a material parameter.

$\tilde{t}$ is a scalar whose sign controls the direction of plastic flow. It takes value of 1 or -1 depends on relative positions of the stress point, σ', on the yield surface and its corresponding image point, $\tilde{\sigma}'$, on the bounding surface.

$M(\theta)$ is calculated as a function of load angle, $\bar{\theta}$, as follows:

$$M(\bar{\theta}) = M\left(\frac{2\alpha^4}{1+\alpha^4-(1-\alpha^4)\sin 3\bar{\theta}}\right)^{\frac{1}{4}} \quad (48)$$

Where load angle $\bar{\theta}$ is defined as:

$$\bar{\theta} = \frac{1}{3}sin^{-1}\left(-\frac{3\sqrt{3}}{2}\frac{J_3}{\sqrt{(J_2)^3}}\right) \quad (49)$$

in which J_2 and J_3 are the second and thrid invariants of the deviatoric stress tensor. Note that the load angle ranges from $\bar{\theta}$=30 for triaxial compression to $\bar{\theta}$=-30 for triaxial extension.

a is determined by below relation:

$$\alpha = \frac{3-sin\varphi_{cs}}{3+sin\varphi_{cs}} \quad (50)$$

M is the value of the critical state stress ratio under triaxial compression which is linked to the critical state friction angle as:

$$M = \frac{6sin\varphi_{cs}}{3-\varphi_{cs}} \quad (51)$$

The direction of plastic flow in this model is calculted based on the following relations:

$$m_g = \frac{\dfrac{\partial g}{\partial \sigma'}}{\left\|\dfrac{\partial g}{\partial \sigma'}\right\|} \quad (52)$$

$\partial g/\partial \sigma'$ is evaluated by applying the chain rule of differentiation as follows:

$$\frac{\partial g}{\partial \sigma'} = \frac{\partial g}{\partial p'}\frac{\partial p'}{\partial \sigma'} + \frac{\partial g}{\partial q}\frac{\partial q}{\partial \sigma'} + \frac{\partial g}{\partial \bar{\theta}}\frac{\partial \bar{\theta}}{\partial \sigma'} \quad (53)$$

(18) Gao et al. [11]:

The following fabric-dependent dilatancy equation was proposed by Gao et al. [11]:

$$d = \frac{d_1}{Mg(\theta)}\left[1+\frac{R}{Mg(\theta)}\right]\left[Mg(\theta)\exp\left(m_1\zeta_g\right) - R\right] \quad (54)$$

whrer d_1 and m_1 are two model constants. ζ_g is defined as follows:

$$\zeta_g = \xi - e_A(A-1)$$

where e_A is a model parameter, ξ=e-e_{cr} is the state parameter, A is a fabric anisotropy variable, R is the sress ratio tensor which is defined as: $R = \sqrt{3/2 r_{ij}r_{ij}}$ in which $r_{ij} = (\sigma_{ij} - p\delta_{ij})/p = s_{ij}/p$, in which σ_{ij} is the stress tensor, p=σ_{ij}/3 is the mean normal stress, δ_{ij} is the Kronecker delta and S_{ij} is the deviator stress. $g(\theta)$ is defined based on the load angle θ as:

$$g(\theta) = \frac{\sqrt{(1+c^2)^2 + 4c(1-c^2)sin3\theta} - (1+c^2)}{2(1-c)sin3\theta} \quad (55)$$

where c=M_e/M_c is the ratio between the critical state stress ratio in triaxial extension M_e and that in triaxial compression M_c.

A is defined based on product of the fabric tensor F_{ij} and the loading direction tensor n_{ij} as:

$$A = F_{ij}n_{ij} \quad (56)$$

where F_{ij} is a symmetric tensor whose norm $F = \sqrt{F_{ij}F_{ij}}$ is named as the degree of fabric.

(19) Qu and Huang [39]:

Similar to Li and Dafalias [29], dilatancy of sand was related to state parameter ξ and the current stress ratio η=q/p' by Qu and Huang [39] as follows:

$$d = \frac{d_0}{M}\left[Mg(\theta)e^{m\xi} - \eta\right] \quad (57)$$

where d_0 and m are material parameters and M is the critical state stress ratio under triaxial compression.

$g(\theta)$ is defined similar to the definition which was given in Gao et al. [11]. θ is the load angle which is defind similar to Kan et al. [21].

Mean effective stress p' and deviatoric stress q are calculated by $p' = I_1/3$ and $q = \sqrt{3J_2}$ in which I_1 is the first invariant of the effective stress tensor and J_2 is the second invariant of the deviatoric stress tensor.

The proposed stress-dilatancy relationship gives rise to the following plastic potential function:

DOI: https://doi.org/10.30564/jgr.v1i2.864

$$g(p',q,p_c) = q + Me^{m\xi}g(\theta)p'ln\left(\frac{p'}{p_c}\right) \quad (58)$$

(20) Jin et al. [20]:

Jin et al. [20] presented the following stress-dilatancy equation for cohesionless sands:

$$d = d_a(M_{PT} - \eta)\, exp\left[h_2(\frac{e}{e_{cr}} - 1)\right] \quad (59)$$

h_2 is a material parameter and d_a is a positive constant which controls the magnitude and evolution of dilatancy rate.

M_{PT} is the current phase transformation stress ratio, η is the current stress ratio, e is the current void ratio, and e_{cr} is the critical state void ratio.

The term (e/e_{cr}-1) is used to adjust dilation or contraction of loose and dense sands. For loose sands $e > e_{cr}$ and $\eta < M_{PT}$, now if $h_2 > 0$ then the exponential term increases the rateof contraction as d_a does. Also if $h_2 < 0$ then the exponential term decreases the rate of contraction. However as shearing continues towards the critical state, the effect of the exponential term on the stress dilatancy diminishes because the exponential term approaches zero. When stress state reaches the critical state, the exponential term totally disappears and $M_{PT}=\eta$ which guarantees zero dilatancy rate at the critical state.

(21) Sun et al. [53]:

Sun et al. [53] investigated the effect of particle breakage on the stress-dilatancy behavior of granular soils and proposed the following plastic flow rule with modification of Rowe's equation:

$$d = \frac{9(M - \eta) + 9\eta\chi}{9 + 3M - 2M\eta - \chi} \quad (60)$$

where

$$\chi = \frac{\gamma(6 + 4M)(3 - M)}{3(6 + M)} \quad (61)$$

in which γ is a material parameter which slightly depends on confining pressure. M is the critical state stress ration under triaxial compression. Therefore, x is a constant.

(22) Yin et al. [70]:

The following simple non-associated plastic potential function was suggested by Yin et al. [70] for very coarse granular materials:

$$g(p',q) = \frac{q}{M_{PT}\, p'} + \ln(p') \quad (62)$$

where $M_{PT} = 6sin\varphi_{PT}/(3 - sin\varphi_{PT})$ in which φ_{PT} is the phase transformation or characteristic angle which corresponds to transition from the contractive to dilative behavior.

(23) Sun and Xiao [52]:

The following plastic potential function was presented for granular soils by Sun and Xiao [52]:

$$g = (2p' - p_o')^2 + (\frac{2q}{M})^2 - P_O'^2 \quad (63)$$

where p_0' controls the size of the plastic potential surface, p' is the mean effective stress, and q is the deviatoric stress.

The following stress-dilatancy relation was also suggested for granular soils by Sun and Xiao [52]:

$$d = \frac{M^2 - (1 - \alpha_d/2)(\eta^2 + M^2)}{\eta^{2-\alpha_d}} \quad (64)$$

where

$$\alpha_d = \exp(\beta_d\xi) \quad (65)$$

in which β_d is a material parameter and ξ is the state parameter.

If the sand is sheared from a dense state where the state parameter is negative ($\xi < 0$), a_d would increase with shearing until the critical state is ultimately reached when $\xi=0$, a_d=1 and d=0. However, if the sand is initially at a loose state where the state parameter is positive ($\xi > 0$), a_d, would decrease until the critical state is reached when $\xi=0$, a_d=1, and d=0.

3.2 Cemented Sands

A summary of the following stress-dilatancy relationships and plastic potential functions of cohesive sands with important highlights is given in table 4 (see appendix section).

(1) Vermeer and De Borst [59]:

Rowe's stress-dilatancy equation in terms of mobilized dilation and friction angle takes the following form [28,59]:

$$sin\psi_m = \frac{sin\varphi_m - sin\varphi_{cv}}{1 - sin\varphi_m sin\varphi_{cv}} \quad (66)$$

where φ_{cv} is the constant volume or critical state friction angle. ψ_m is the mobilized dilatancy angle which is a function of plastic strain as the mobilized friction angle (φ_m) does. Thus, change in ψ_m can be predicted by change in φ_m.

The above equation was initially proposed by Vermeer and De Borst [59] for soils, rocks and concrete. However,

 DOI: https://doi.org/10.30564/jgr.v1i2.864

this form of Rowe's equation can not describe the density or void ratio dependency during shearing. In order to address this shortcoming, a modification of the original Rowe's equation was proposed by Wan and Guo [60] as follows:

$$sin\psi_m = \frac{sin\varphi_m - (e/e_{cr})^{\omega_d}\, sin\varphi_{cv}}{1 - (e/e_{cr})^{\omega_d}\, sin\varphi_m sin\varphi_{cv}} \tag{67}$$

where e is the current void ratio, e_{cr} is the critical state void ratio, and ω_d is a material parameter. Parameter ω_d can also be linked to fabric tensor, plastic shear strain and the effect of intermediate principal stress measured by parameter $b = (\sigma_2 - \sigma_3)/(\sigma_1 - \sigma_3)$ [60].

(2) Kim and Lade [24]:

Based on variety of experimental observations, Kim and Lade [24] suggested the following equation for the plastic potential function of cohesive and non-cohesive frictional materials:

$$g(I_1, I_2, I_3) = \left(\psi_1 \frac{I_1^3}{I_3} - \frac{I_1^2}{I_2} + \psi_2\right)\left(\frac{I_1}{p_a}\right)^{\mu} \tag{68}$$

where ψ_1, ψ_2, and μ are the plastic potential parameters, p_a is the atmospheric pressure and I_1, I_2, and I_3 are the first, second, and third invariant of the stress tensor which are defined based on the three principal stresses (observed during triaxial tests) as follows [24]:

$$I_1 = \sigma_1 + \sigma_2 + \sigma_3 \tag{69}$$

$$I_2 = -(\sigma_1.\sigma_2 + \sigma_2.\sigma_3 + \sigma_3.\sigma_1) \tag{70}$$

$$I_3 = \sigma_1.\sigma_2.\sigma_3 \tag{71}$$

Reddy and Saxena [45], Lade and Kim [26], Kandasami et al. [22], Singh et al. [50], and Singh et al. [51] used the above plastic potential function in their constitutive model to simulate the plastic flow of cemented and uncemented geomaterials.

(3) Van den Hoek and Geilikman [58]:

Van den Hoek and Geilikman [58] presented the following plastic potential function for sandstone in analysis of sand production in petroleum wells:

$$g = \frac{1}{2}(\sigma_\vartheta^{'} - \sigma_r^{'}) - \frac{1}{2}(\sigma_\vartheta^{'} + \sigma_r^{'})sin\psi + constant \tag{72}$$

where ψ is the dilation angle, $\sigma_\vartheta^{'}$ is the tangential effective stress and $\sigma_r^{'}$ is the radial effective stress. Constant value has no impact on the model since only the derivative of the plastic potential function is influential in constitutive model.

(4) Arroyo et al. [3]:

Arroyo et al. [3] proposed the following stress-dilatancy equation for cemented sands:

$$d = m_g(M - \eta)\left(\frac{a_g M}{\eta}\right) \tag{73}$$

where m_g, a_g, and M are model parameters which control the shape of the plastic potential surface.

Note that the above stress-dilatancy relationship is similar to that presented by Lagioia et al. [27]. Buscarnera and Laverack [5] also used the similar flow rule as above in their constitutive model presented for porous rocks.

(5) Yu et al. [73]:

The following stress-dilatancy relationship was proposed by Yu et al. [73] for cemented soils:

$$d = \frac{9(M - \eta) + 6\frac{coh}{p^{'}}\sqrt{(2M + 3)(-M + 3)}}{9 + 3M - 2M\eta + 4\frac{coh}{p^{'}}\sqrt{(2M + 3)(-M + 3)}} \tag{74}$$

where coh is the interparticle cohesion. Original Rowe's flow rule can be recovered by setting $coh=0$. In this model, cohesion was assumed to degrade with the total plastic strain increment as follows:

$$dcoh = coh\exp\left(-\varpi.\sqrt{(\dot{\varepsilon}_q^p)^2 + (\dot{\varepsilon}_p^p)^2}\right) \tag{75}$$

where ϖ determines rate of cohesion degradation.

The plastic potential function corresponds to the above stress-dilatancy equation is as follows [73]:

$$g = 3M\, ln\left(\frac{p^{'} + p_t^{'} - k_g}{\varphi_g}\right) + (2M + 3)\, ln\left(\frac{2(q - h_g)}{p^{'} + p_t^{'} - k_g} + 3\right) + (M - 3)ln\left(3 - \frac{q - h_g}{p^{'} + p_t^{'} - k_a}\right) \tag{76}$$

$$k_g = \frac{\sqrt{(3 + 2M)(3 - M)}\,(36 - 12M)coh}{18M^2 - 27M - 81} \tag{77}$$

$$h_g = \frac{\sqrt{(3 + 2M)(3 - M)}\,(-54 + 18M)coh}{18M^2 - 27M - 81} \tag{78}$$

Rahimi et al. [41], Rahimi et al. [42] and Rahimi et al. [44] used the same stress-dilatancy relationship as that proposed by Yu at al. [73] by replacement of constant critical state stress ratio with variable phase transformation stress

DOI: https://doi.org/10.30564/jgr.v1i2.864

ratio.

(6) Wang and Leung [63]:

Wang and Leung [63] presented the following stress-dilatancy relationship for cemented sands in triaxial condition (i.e. an axisymmetric condition):

$$q\dot{\varepsilon}_q^p + p^{'}\dot{\varepsilon}_P^p = Mp^{'}\dot{\varepsilon}_q^p + \Delta W_{bond} \tag{79}$$

or

$$\frac{q}{p^{'}} + \frac{\dot{\varepsilon}_P^p}{\dot{\varepsilon}_q^p} = M + \frac{\Delta W_{bond}}{p^{'}\dot{\varepsilon}_q^p} \quad or \quad d = M - \eta + \frac{\Delta W_{bond}}{p^{'}\dot{\varepsilon}_q^p} \tag{80}$$

where ΔW_{bond} is the total energy which is dissipated due to breakage or destruction of the cementing bond.

Ajorloo et al. [1] also suggested the same stress-dilatancy relation for cemented sands. However, neither Wang and Leung [63] nor Ajorloo et al. [1] did not put forward any formulas for .ΔW_{bond} Suggestion of any relationship for ΔW_{bond} will be considered as a contribution for the stress-dilatancy relation of cemented sands.

(7) Zhang and Salgado [74]:

Since original Rowe's stress-dilatancy relationship does not produce correct volumetric response for cemented materials [73, 74, 40, 41], a modification of Rowe's equation was proposed by Zhang and Salgado [74] as follows to address this deficiency:

$$\frac{\sigma_1^{'}}{\sigma_3^{'}} = K\left(1 - \frac{\dot{\varepsilon}_V}{\dot{\varepsilon}_1}\right) + \frac{2coh}{\sigma_3^{'}}K\sqrt{1 - \frac{\dot{\varepsilon}_V}{\dot{\varepsilon}_1}} \tag{81}$$

where K is a parameter which depends on the failure friction angle, $\sigma_1^{'}$ and $\sigma_3^{'}$ are the major and minor principal effective stresses, respectively, $\dot{\varepsilon}_V$ and $\dot{\varepsilon}_1$ are the volumetric and major principal strain increment.

The above equation can be written in terms of the mean effective stress $p^{'}$, the deviator stress q, and the critical state stress ratio under compression M as follows:

$$d = \frac{9(M - \eta) - 3m_c}{9 + 3M - 2\eta M + m_c} \tag{82}$$

where m_c is related to the cohesion as follows:

$$m_c = \frac{6(-M+3)\left(coh/p^{'}\right)^2}{-\eta+3} - \frac{2coh(-M+3)}{p^{'}}\sqrt{\left(\frac{3coh/p^{'}}{-\eta+3}\right)^2 + \frac{2\eta+3}{-\eta+3}} \tag{83}$$

Where *coh* is the interparticle cohesion.

Note that Zhang and Salgado [74] and Yu et al. [72,73]'s stress-dilatancy relationships have been mentioned in Porcino and Marciano [38] as well.

(8) Gao and Zhao [10]:

Gao and Zhao [10] presented the following flow rule for cemented sands:

$$d = \frac{d_1}{exp\left(\int \langle dL \rangle\right)}\left(M_{PT}d_C d_F - H\right) \tag{84}$$

where d_1 is a positive model parameter, M_{PT} is the phase transformation stress ratio, H is hardening parameter, DL is a loading index and $\langle x \rangle$ denotes the Macauley bracket with $\langle x \rangle$=0 when $x \leq 0$ and $\langle x \rangle = x$ when $x > 0$. The role of the denominator in above equation is to control the volume change, especially when the strain level is high. As the sample is sheared to the critical state, the increment of the plastic deviatoric strain is unlimited. At this state, the denominator term will reach infinity making the value of the dilatancy rate d zero. The two parameters d_C and d_F are used to characterize the bonding and anisotropic effects, respectively, as follows:

$$d_C = exp\left(-c_0\sqrt{\frac{\sigma_0}{p_r}}\right) \tag{85}$$

$$d_F = exp(k(A+1)) \tag{86}$$

where C_0 and k are positive model constants, σ_0 denotes the current triaxial tensile strengthof the material, p_r is a reference pressure and A is an anisotropic variable dependent on fabric tensor whose definition has given in Gao and Zhao [10].

Above equations imply that as the value of tensile strength increases, d_C decreases which leads to reduction in value of the dilatancy rate d. The material response is less contractive and hence the liquefaction resistant increases. Also d_F increases with A (the major principal stress direction becomes closer to the direction of deposition) which in turn results in larger value of the dilatancy rate d and hence more contractive response and less resistant to the liquefaction [10].

(9) Weng [65]:

In his generalized plasticity model for sandstone, Weng [65] used Nova and Wood [36]'s stress-dilatancy relationship which has been proposed for cohesionless sands. This, however, is a questionable choice because cemented sands show more dilative behavior than uncemented sands [40, 41]. This can not be reproduced simply by using the flow rule developed for cohesionless sands.

(10) Rios et al. [46]:

Rios et al. [46] applied Rowe's stress-dilatancy relation (equation 10) in their constitutive model developed for modelling bonded soils. This is controversial. As men-

 DOI: https://doi.org/10.30564/jgr.v1i2.864

tioned already, the stress-dilatancy relationships proposed for cohesionless sands do not work for cemented or bonded sands because volumetric behavior of uncemented sands is different than that of cemented sands [40, 41].

4. Conclusion

Some important stress-dilatancy relationships and plastic potential functions proposed for uncemented and cemented sands were reviewed in this article. The paper suggests that unlike uncemented sands for which intensive research has been performed by different researchers, there are a few researches on the stress-dilatancy relationships of cemented sands. To fill this gap, considerable effort is needed. Therefore, it is recommended that this area (stress-dilatancy relationship of cemented sands) is chosen as a potential research title for future studies. Modification of Rowe's equation can be a step forward to account for deficiencies of the previous stress-dilatancy relationships proposed for cemented sands.

Conflicts of interest

The corresponding author confirms that there is no conflict of interest.

Appendix

Summary of aforementioned flow rule and plastic potential equations for uncemented and cemented sands

Table 3. Summary of proposed stress-dilatancy and plastic potential relationships for uncemented sands

Proposed stress-dilatancy relationship or plastic potential function	Methodology/Application/Validation (Calibration)
Nova and Wood [35]	-proposed on the basis of experimental works on sand in plane strain & triaxial conditions. -when μ=1, the equation reduces to that of the Cam Clay model. -verified against constant p' and constant q laboratory tests with great matches.
Nova and Wood [36]	-One of the oldest and most popular stress-dilatancy relationships. -This relationship has been employed by many researchers like Pastor et al. [37], Haeri and Hamidi [13], Hamidi and Yarbakhti [14] and Kong et al. [25].
Jefferies [17]	-proposed in his critical state constitutive model. -when N=0, the equation reduces to the familiar Cam Clay model. -the influence of void ratio and mean effective stress on sand response is captured well but the influence of fabric is neglected.
Lagioia et al.[27]	-proposed such that it predicts zero dilatancy rate in the critical state and infinite dilatancy rate in zero stress ratio. -verified against drained triaxial tests with excellent matches.
Yu [71]	-proposed for both sand & clay based on Rowe's stress-dilatancy relationship. -verified against drained & undrained triaxial compression tests of sand & clay with very good agreements.
Schanz et al. [15]	-proposed based on concept of mobilized dilatancy angle, mobilized friction angle and critical state friction angle. -the mobilized friction angle is estimated by shape of a Mohr-Coulomb failure envelope. -calibrated for drained & undrained behavior of Hostun loos sand under oedometer & triaxial tests.
Wan and Guo [61]	-a fabric dependent stress-dilatancy equation. -successfully calibrated against undrained & drained behavior of Ottawa & Toyoura sands.
McDowell [31]	-the flow rule is non-associated. Hence, the critical state point does not happen at the top of yield surface. -fulfills the necessary conditions of zero shear strain under isotropic conditions and infinite shear strain with zero volumetric strain at the critical state. This approach is identical to that suggested by Lagioia et al. [27] -performance of the model was discussed, however, it was not verified against experimental observations.
Russell and Khalili [48]	-A state parameter dependent stress-dilatancy equation within critical state framework. -Comparison of predicted volumetric behavior with experimental results (under isotropic & oedometric compression, and drained & undrained triaxial tests) suggests a great credit for the proposed equation.
Dafalias and Manzari [33]	-a fabric dependent stress-dilatancy equation based on difference between the current stress ratio and the phase transformation stress ratio. -The model predicts a phase transformation stress ratio equal to the current stress ratio at the critical state which results in zero dilatancy rate (permanent steady state response). -calibrated against drained & undrained monotonic & cyclic compression tests. Predicted volumetric responses were in very good harmony with experimentally measured behaviors.
Khalili et al. [23]	-similar to equation of Russell and Khalili [48]. -validated excellently against drained & undrained compression monotonic & cyclic tests on loose & dense samples of Hostun sand.
Imam et al. [16]	-similar to equation of Dafalias and Manzari [33], however, it is not fabric dependent. -proposed for both triaxial compression and triaxial extension. -volumetric response was validated against many drained & undrained triaxial compression & extension tests on Ottawa and Toyoura sands under monotonic loading with appreciable matches.
Ling and Yang [30]	-a combination of relationships proposed by Nova and Wood [36] and Li and Dafalias [29]. -a variable stress ratio (M_f) is used in this equation rather than the constant critical state stress ratio (M). -wondeful performance of the equation was proved by calibration of drained & undrained volumetric behavior of Toyoura & Nevada & Fuji River sands under monotonic & cyclic loading.

DOI: https://doi.org/10.30564/jgr.v1i2.864

Sasiharan [49]	-a fabric dependent equation. -Similar to Jefferies's approach, Sasiharan considered the resulting plastic potential function, obtained by integration of the flow rule, identical to the yield function. -calibrated against drained & undrained triaxial compression tests under monotonic & cyclic loading with good matches.
Tasiopoulou and Gerolymos [55]	-a hardening parameter & phase transformation stress ratio dependent equation. -performance of the model was examined but it was not validated against experimental observations.
Kan et al. [21]	-a relatively complex equation for plastic potential function. -calibrated successfully against drained & undrained cyclic tests on loose & dense samples of Toyoura & Fuji River sands.
Gao et al. [11]	-a relatively complex fabric-dependent dilatancy equation. -calibrated against drained & undrained behavior of Toyoura & Fraser River sands under different loading conditions.
Qu and Huang [39]	-a state parameter dependent dilatancy equation. -was not verified based on experimental observations.
Jin et al. [20]	-a void ratio & phase transformation stress ratio dependent equation. -calibrated based on drained & undrained triaxial compression tests of Nevada & Toyoura sands under monotonic & cyclic loading.
Sun et al. [53]	-a modified version of Rowe's equation which considers the effect of particle breakage. -was calibrated against plastic flow of Yixing rockfill, Kish Island & Cambria sands
Yin et al. [70]	-a simple non-associated plastic potential function suggested for very coarse granular materials. -calibrated based on drained triaxial tests on rockfill materials with different grain sizes.
Sun and Xiao [52]	-a state parameter dependent dilatancy equation for granular soils subjected to monotonic triaxial compression. -calibrated successfully against drained & undrained triaxial compression tests on various granular soils.

Table 4. Summary of proposed stress-dilatancy and plastic potential relationships for cemented sands

Proposed stress-dilatancy relationship or plastic potential function	Methodology/Application/Validation (Calibration)
Vermeer and De Borst [59]	-Rowe's stress-dilatancy equation in terms of mobilized dilation and friction angles. -proposed for soils, rocks and concrete. -a modified version that takes into account the density or void ratio dependency during shearing was proposed by Wan and Guo [60].
Kim and Lade [24]	-a plastic potential function for cohesive and non-cohesive frictional materials proposed based on many experimental observations.
Van den Hoek and Geilikman [58]	-a plastic potential function proposed for analysis of sand production in petroleum wells. -sand production analysis was performed, however, volumetric behavior of sandstone was not calibrated against physical tests.
Arroyo et al. [3]	-flow rule similar to that of Lagioia et al. [27]. -no strong validation against physical tests.
Yu et al. [73]	-a modified version of Rowe's flow rule proposed for modelling bonded geomaterials. -satisfactory agreement of volumetric behavior for numerical and physical tests. Also no validation was performed for undrained tests.
Wang and Leung [63]	-proposed for cemented sands under triaxial condition (i.e. an axisymmetric condition): -no calibration was done to validate the proposed flow rule.
Zhang and Salgado (2010)	- a modification of Rowe's equation -no verification against experimental observations.
Gao and Zhao [10]	-a fabric anisotropy dependent stress-dilatancy relationship. -successful calibration of volumetric behavior of cemented Ottawa sand in drained triaxial compression & Toyoura sand in drained true triaxial tests. -no validation against undrained tests.
Weng [65]	-identical to Nova and Wood [36]'s stress-dilatancy equation. -arguable choice because cohesive sands show more dilative response than uncemented sands.
Rios et al. [46]	-identical to Rowe's stress-dilatancy equation. -controversial since volumetric behavior of uncemented sands is different than that of cohesive sands.

References

[1] Ajorloo, A. M., Mroueh, H., & Lancelot, L.. Experimental investigation of cement treated sand behavior under triaxial test. Geotechnical and Geological Engineering, 2012, 30(1): 129-143.

[2] Andrade, J. E.. A predictive framework for liquefaction instability. Géotechnique, 2009, 59(8): 673.

[3] Arroyo, M., Castellanza, R., & Nova, R.. Compaction bands and oedometric testing in cemented soils. Soils and foundations, 2005, 45(2): 181-194.

[4] Been, K., & Jefferies, M.. Stress dilatancy in very loose sand. Canadian Geotechnical Journal, 2004, 41(5): 972-989.

[5] Buscarnera, G., & Laverack, R. T.. Path dependence of the potential for compaction banding: Theoretical predictions based on a plasticity model for porous rocks. Journal of Geophysical Research: Solid Earth, 2014, 119(3): 1882-1903.

[6] Chang, C. S., & Yin, Z. Y.. Modeling stress-dilatancy for sand under compression and extension loading conditions. Journal of engineering mechanics, 2009, 136(6): 777-786.

[7] Chu, J., Kim, S. R., Oh, Y. N., Balasubramaniam, A. S., & Bergado, D. T.. An experimental and theoretical study on the dilatancy of sand and clays. In Proceedings of the 9th Australia–New Zealand. Conference on geomechanics, 2004, 2: 654-660.

[8] Cui, Y. J., & Delage, P.. Yeilding and plastic be-

 DOI: https://doi.org/10.30564/jgr.v1i2.864

haviour of an unsaturated compacted silt. Géotechnique, 1996, 46(2): 291-311.

[9] DeSimone, A., & Tamagnini, C.. Stress–dilatancy based modelling of granular materials and extensions to soils with crushable grains. International journal for numerical and analytical methods in geomechanics, 2005, 29(1): 73-101.

[10] Gao, Z., & Zhao, J.. Constitutive modeling of artificially cemented sand by considering fabric anisotropy. Computers and Geotechnics, 2012, 41: 57-69.

[11] Gao, Z., Zhao, J., Li, X. S., & Dafalias, Y. F.. A critical state sand plasticity model accounting for fabric evolution. International journal for numerical and analytical methods in geomechanics, 2014, 38(4): 370-390.

[12] Gutierrez, M., Ishihara, K., & Towhata, I.. Model for the deformation of sand during rotation of principal stress directions. Soils and Foundations, 1993, 33(3), 105-117.

[13] Haeri, S. M., & Hamidi, A.. Constitutive modelling of cemented gravelly sands. Geomechanics and Geoengineering: An International Journal, 2009, 4(2): 123-139.

[14] Hamidi, A., & Yarbakhti, P.. Constitutive modeling of cemented gravely sands including the effects of cement type. Journal of Engineering Geology, 2013, 6(2): 1525-1544.

[15] Imam, S. M. R.. Modeling the constitutive behavior of sand for the analysis of static liquefaction, 1999.

[16] Imam, S. R., Morgenstern, N. R., Robertson, P. K., & Chan, D. H.. A critical-state constitutive model for liquefiable sand. Canadian geotechnical journal, 2005, 42(3): 830-855.

[17] Jefferies, M. G.. Nor-Sand: a simple critical state model for sand. Geotechnique, 1993, 43(1): 91-103.

[18] Jefferies, M., & Been, K.. Soil liquefaction: a critical state approach. CRC press, 2015.

[19] Jefferies, M. G., & Shuttle, D. A.. Dilatancy in general Cambridge-type models. Géotechnique, 2002, 52(9): 625-638.

[20] Jin, Y., Yin, Z., Zhang, D., & Huang, H.. Unified modeling of the monotonic and cyclic behaviors of sand and clay. Acta Mechanica Solida Sinica, 2015, 28(2): 111-132.

[21] Kan, M. E., Taiebat, H. A., & Khalili, N.. Simplified mapping rule for bounding surface simulation of complex loading paths in granular materials. International Journal of Geomechanics, 2013, 14(2): 239-253.

[22] Kandasami, R. K., Singh, S., & Murthy, T. G.. Calibration and validation of Lade's constitutive model for weakly cemented sands, 2016.

[23] Khalili, N., Habte, M. A., & Valliappan, S.. A bounding surface plasticity model for cyclic loading of granular soils. International journal for numerical methods in engineering, 2005, 63(14): 1939-1960.

[24] Kim, M. K., & Lade, P. V.. Single hardening constitutive model for frictional materials: I. Plastic potential function. Computers and Geotechnics, 1988, 5(4): 307-324.

[25] Kong, X., Liu, J., Zou, D., & Liu, H.. Stress-dilatancy relationship of Zipingpu gravel under cyclic loading in triaxial stress states. International Journal of Geomechanics, 2016, 16(4): 04016001.

[26] Lade, P. V., & Kim, M. K.. Single hardening constitutive model for soil, rock and concrete. International Journal of Solids and Structures, 1995, 32(14): 1963-1978.

[27] Lagioia, R., Puzrin, A. M., & Potts, D. M.. A new versatile expression for yield and plastic potential surfaces. Computers and Geotechnics, 1996, 19(3): 171-191.

[28] Li, H. Z., Xiong, G. D., & Zhao, G. P.. An elasto-plastic constitutive model for soft rock considering mobilization of strength. Transactions of Nonferrous Metals Society of China, 2016, 26(3): 822-834.

[29] Li, X. S., & Dafalias, Y. F.. Dilatancy for cohesionless soils. Geotechnique, 2000, 50(4): 449-460.

[30] Ling, H. I., & Yang, S.. Unified sand model based on the critical state and generalized plasticity. Journal of Engineering Mechanics, 2006, 132(12): 1380-1391.

[31] McDowell, G. R.. A simple non-associated flow model for sand. Granular Matter, 2002, 4(2): 65-69.

[32] Liu, J., Zou, D., Kong, X., & Liu, H.. Stress-dilatancy of Zipingpu gravel in triaxial compression tests. Science China Technological Sciences, 2016, 59(2): 214-224.

[33] Manzari, M. T., & Dafalias, Y. F.. A critical state two-surface plasticity model for sands. Geotechnique, 1997, 47(2): 255-272.

[34] Muhunthan, B., & Sasiharan, N.. Fabric dilatancy and the plasticity modeling of granular media. International Journal for Numerical and Analytical Methods in Geomechanics, 2012, 36(9): 1181-1193.

[35] Nova, R., & Wood, D. M.. A constitutive model for sand in triaxial compression. International Journal for Numerical and Analytical Methods in Geomechanics, 1979, 3(3): 255-278.

[36] Nova, R., & Wood, D. M.. A constitutive model for soil under monotonic and cyclic loading. Soil mechanics-transient and cyclic loading, 1982: 343-373.

[37] Pastor, M., Zienkiewicz, O. C., & Leung, K. H.. Simple model for transient soil loading in earthquake analysis. II. Non-associative models for sands. Inter-

DOI: https://doi.org/10.30564/jgr.v1i2.864

national Journal for Numerical and Analytical Methods in Geomechanics, 1985, 9(5): 477-498.

[38] Porcino, D. D., & Marcianò, V.. Bonding degradation and stress–dilatancy response of weakly cemented sands. Geomechanics and Geoengineering, 2017, 1-13.

[39] Qu, X., & Huang, M.. Numerical Simulation of Static Liquefaction of Loose Sand. In Soil Behavior and Geomechanics, 2014: 587-595.

[40] Rahimi, M.. Constitutive Modeling of Soft Sandstone Degradation under Cyclic Conditions, Doctoral dissertation, University of Alberta, 2014.

[41] Rahimi, M., Chan, D., & Nouri, A.. Bounding surface constitutive model for cemented sand under monotonic loading. International Journal of Geomechanics, 2015, 16(2): 04015049.

[42] Rahimi, M., Chan, D., Nouri, A., & Rasouli, R.. Effects of inherent fabric anisotropy and intermediate principal stress on constitutive behavior of uncemented and cemented sands. Computers and Geotechnics, 2016, 80: 237-247.

[43] Rahimi, M., Chan, D., & Nouri, A.. Constitutive model for cyclic behaviour of cohesionless sands. Geomechanics and Geoengineering, 2017, 12(1): 36-47.

[44] Rahimi, M., Chan, D., & Nouri, A.. Constitutive model for monotonic and cyclic responses of loosely cemented sand formations. Journal of Rock Mechanics and Geotechnical Engineering, ,2018, 10(4): 740-752.

[45] Reddy, K. R., & Saxena, S. K.. Constitutive modeling of cemented sand. Mechanics of materials, 1992, 14(2): 155-178.

[46] Rios, S., Ciantia, M., Gonzalez, N., Arroyo, M., & da Fonseca, A. V.. Simplifying calibration of bonded elasto-plastic models. Computers and Geotechnics, 2016, 73: 100-108.

[47] Rowe, P. W.. The stress-dilatancy relation for static equilibrium of an assembly of particles in contact. In Proceedings of the royal society of London a: mathematical, physical and engineering sciences. The Royal Society, 1962, 269(1339): 500-527.

[48] Russell, A. R., & Khalili, N.. A bounding surface plasticity model for sands exhibiting particle crushing. Canadian Geotechnical Journal, 2004, 41(6): 1179-1192.

[49] Sasiharan, N.. Mechanics of dilatancy and its application to liquefaction problems, 2006, 68(02).

[50] Singh, S., Kandasami, R. K., & Murthy, T. G.. Prediction of mechanical response of geomaterials using an advanced elasto-plastic constitutive model. Procedia Engineering, 2017a, 173: 793-799.

[51] Singh, S., Kandasami, R. K., & Murthy, T. G.. Mechanics and modeling of cohesive frictional granular materials. In Advances in Laboratory Testing and Modelling of Soils and Shales, Springer, Cham, 2017b: 493-500.

[52] Sun, Y., & Xiao, Y.. Fractional order plasticity model for granular soils subjected to monotonic triaxial compression. International Journal of Solids and Structures, 2017.

[53] Sun, Y., Xiao, Y., & Ji, H.. Dilation and breakage dissipation of granular soils subjected to monotonic loading. Acta Mechanica Sinica, 2016, 32(6): 1065-1074.

[54] Szypcio, Z.. Stress-dilatancy for soils. Part I: The frictional state theory. Studia Geotechnica et Mechanica, 2016, 38(4): 51-57.

[55] Tasiopoulou, P., & Gerolymos, N.. Development of a modified elastoplasticity model for sand. In Proceedings of the second international conference on performance–based design in earthquake geotechnical engineering, Taormina (Italy), CD Rom, 2012: 28-30.

[56] Tasiopoulou, P., & Gerolymos, N.. Constitutive modeling of sand: Formulation of a new plasticity approach. Soil Dynamics and Earthquake Engineering, 2016, 82: 205-221.

[57] Taylor, D. W.. Fundamentals of soil mechanics, Wiley, New York, 1948.

[58] Van den Hoek, P. J., & Geilikman, M. B.. Prediction of sand production rate in oil and gas reservoirs. In SPE Annual Technical Conference and Exhibition. Society of Petroleum Engineers, 2003.

[59] Vermeer, P. A., & De Borst, R.. Non-associated plasticity for soils, concrete and rock. HERON, 1984, 29 (3).

[60] Wan, R. G., & Guo, P. J.. A simple constitutive model for granular soils: modified stress-dilatancy approach. Computers and Geotechnics, 1998, 22(2): 109-133.

[61] Wan, R. G., & Guo, P. J.. Effect of microstructure on undrained behaviour of sands. Canadian Geotechnical Journal, 2001, 38(1): 16-28.

[62] Wang, J.. The stress-strain and strength characteristics of Portaway Sand, Doctoral dissertation, University of Nottingham, 2005.

[63] Wang, Y. H., & Leung, S. C.. Characterization of cemented sand by experimental and numerical investigations. Journal of geotechnical and geoenvironmental engineering, 2008, 134(7): 992-1004.

[64] Wang, Z. L., Dafalias, Y. F., Li, X. S., & Makdisi, F. I.. State pressure index for modeling sand behavior. Journal of geotechnical and geoenvironmental engi-

 DOI: https://doi.org/10.30564/jgr.v1i2.864

neering, 2002, 128(6): 511-519.

[65] Weng, M. C.. A generalized plasticity-based model for sandstone considering time-dependent behavior and wetting deterioration. Rock Mechanics and Rock Engineering, 2014, 47(4): 1197-1209.

[66] Wood, D. M.. Soil behaviour and critical state soil mechanics. Cambridge university press, 1990.

[67] Yao, Y. P., Sun, D. A., & Luo, T.. A critical state model for sands dependent on stress and density. International Journal for Numerical and Analytical Methods in Geomechanics, 2004, 28(4): 323-337.

[68] Yao, Y. P., Sun, D. A., & Matsuoka, H.. A unified constitutive model for both clay and sand with hardening parameter independent on stress path. Computers and Geotechnics, 2008, 35(2): 210-222.

[69] Yin, Z. Y., & Chang, C. S.. Stress–dilatancy behavior for sand under loading and unloading conditions. International Journal for Numerical and Analytical Methods in Geomechanics, 2013, 37(8): 855-870.

[70] Yin, Z. Y., Hicher, P. Y., Dano, C., & Jin, Y. F.. Modeling mechanical behavior of very coarse granular materials. Journal of Engineering Mechanics, 2016, 143(1): C4016006.

[71] Yu, H. S.. CASM: A unified state parameter model for clay and sand. International Journal for Numerical and Analytical Methods in Geomechanics, 1998, 22(8): 621-653.

[72] Yu, H. S., Khong, C., & Wang, J.. A unified plasticity model for cyclic behaviour of clay and sand. Mechanics research communications, 2007a, 34(2): 97-114.

[73] Yu, H. S., Tan, S. M., & Schnaid, F.. A critical state framework for modelling bonded geomaterials. Geomechanics and Geoengineering, 2007b, 2(1): 61-74.

[74] Zhang, J., & Salgado, R.. Stress-dilatancy relation for Mohr-Coulomb soils following a non-associated flow rule. Geotechnique, 2010.

DOI: https://doi.org/10.30564/jgr.v1i2.864

BILINGUAL PUBLISHING CO.
Pioneer of Global Academics Since 1984

Journal of Geological Research
https://ojs.bilpublishing.com/index.php/jgr-a

ARTICLE

Living Matter and the Laws of Thermodynamics for the Biosphere

Nabil H. Swedan*

Pacific Engineering PLLC, Redmond, WA, 98052, U.S.A.

ARTICLE INFO

Article history
Received: 14 May 2019
Accepted: 25 June 2019
Published Online: 30 July 2019

Keywords:
Laws of Thermodynamics
Biosphere
Photosynthesis
Past climates
Surface geology

ABSTRACT

The laws of thermodynamics have been developed for inert matter, and living matter has not been considered as a variable in these laws. Living matter possesses properties that have had major effects on biosphere evolution with time. The zeroth property is "Living matter is produced from living matter only." The first property may be summarized as "Living matter occupies the available spaces to the maximum extent when environmental conditions are favorable and no obstacles are present." And the second property is " Living matter mutates, changes, and adapts to maintain the continuity of life and size as large as possible when environmental conditions are unfavorable." While the zeroth property is objective in nature, the first and second properties are subjective, in that they are driven by internal stimuli characterizing living matter. Their interaction with the laws of thermodynamics may be thought of as "philosophy intertwining with science." Accordingly, the laws of thermodynamics are revised to factor in life as a variable. Mathematical expressions of the first and second laws are derived and some of their applicability to the biosphere and climate is explained and discussed. The main conclusion is that life changes climates and the fabric of the biosphere.

1. Introduction

Planetary motion is characterized by conservation of the angular momentum and infinitesimal variation of orbital eccentricity. These characteristics yield a constant annual solar energy exchanged with any planet, regardless of orbit shape. A planet thus reaches thermodynamic equilibrium. Seasonal or orbital variations induce thermodynamic transformations displaced differentially from equilibrium. They are, therefore, reversible based on the laws of thermodynamics, and lifeless planets may not have relevant directional thermodynamic transformations.

This is not what is observed on planet earth. The geological record is rich with data revealing steady evolution of living matter, surface geology, and climate. Clearly, life on earth has made a difference, and the first and second laws of thermodynamics must be revised for the biosphere. This sphere includes living and inert matters that interact with each other, and this interaction was not accounted for in the original formulation of the laws of thermodynamics. They were developed for practical applications, where systems' surroundings are part of the biosphere such as land, air, and water. The entire system and its surroundings were made of inert matter. Conversely, biosphere thermodynamic transformations are interactions between living and inert matters, and they changed climates of the past as well as present-day climates.

The biosphere as a thermodynamic system where living and inert matters interact comprises land, surface water,

**Corresponding Author:*
Nabil H. Swedan,
Pacific Engineering PLLC, 9350 Redmond Woodinville Road NE, B210, Redmond, WA, 98052, U.S.A;
Email: nabilswedan2@gmail.com ; swedan@pacificengineeringpllc.com

 DOI: https://doi.org/10.30564/jgr.v1i2.1007

living matter in the sea and on the land, and atmospheric air. These biosphere subsystems observe biological, chemical, and thermodynamic changes with variation in the size of life. Because the size of the non-green living matter depends on the size of the green matter, variation in the size of life is equal to variation in the chemical energy of photosynthesis. An increase in the size of photosynthesis converts more solar energy into chemical energy in plant tissues and the surroundings receive less solar energy and vice versa. Consequently, photosynthesis exchanges heat that is in transit in the biosphere and may be treated as such. Therefore, the first property of living matter intertwines with the first law of thermodynamics. So does the second property: Unlike lifeless planets, biosphere thermodynamic transformations have a steady direction, irreversible, and the second law of thermodynamics must be revised as well.

In this work, the interactions of the basic properties of living matter and the laws of thermodynamics are discussed, derivation of the revised laws of thermodynamics to account for life in the biosphere is provided, and the significance of the derived laws is explained.

2. Background Information

The zeroth and first properties of living matter were proposed and thoroughly discussed by [1]. There is overwhelming evidence of their validity. Not a single living cell that eats, secretes, and multiplies has been produced in laboratory experiments. Nor is there evidence of living cells being a product of purely inert matter. Such overwhelming evidence is a reasonable basis to claim that "Living matter is produced from living matter only." Similarly, our basic observations indicate that living matter has an inherent and intrinsic nature to multiply and increase in number when the conditions are favorable and no obstacles are present. This is true for single living cells as well as complex organisms, and there is overwhelming proof of the validity of this conclusion as well.

The innate nature of living matter to adapt, change, and mutate when environmental conditions are unfavorable or vary is observed throughout the geological record. Bacteria mutation in response to medicine and subsequent resistance maintains the continuity of life and bacteria count to the maximum extent. Also, this is true for plants, insects, animals, and humans. Plants adapt, change, produce venoms, lignin, and rise above the ground to occupy the available spaces as much as practically possible. Variation in climates with latitude has produced fauna and flora characteristic of each latitude. Plants shed their leaves in cold climates to maintain the continuity of their existence. The evidence that "Living matter mutates, changes, and adapt to maintain the continuity of life and size as large as possible when environmental conditions are unfavorable" is overwhelming as well. These inherent natural properties of living matter exchange energy that interacts with the thermodynamics of the biosphere. Therefore, they must be accounted for in the laws of thermodynamics.

Thermodynamics is an established branch of science that addresses transformations where heat and work are exchanged between thermodynamic systems and their surroundings. Reference [2] presents the current understanding of thermodynamics applicable to systems involving inert matter only. " Postulate 1: *There exists a form of energy known as internal energy U, which for systems in equilibrium states is an intrinsic property of the system, functionally related to the measurable coordinates which characterizes the system.* Postulate 2: *the total energy of any system and its surroundings is conserved*. (First law of thermodynamics)." Mathematically, this law may be written as follows:

$$dU=dQ-dW \quad (1)$$

Where Q is heat crossing the boundary of the thermodynamic system. The convention is to consider the heat as positive if added to the thermodynamic system. The symbol, W, denotes the work exchanged between system and surroundings. It is energy in transit as well, typically assumed as positive if produced by the thermodynamic system. Therefore, Q and W have opposite signs.

"Postulate 3: *There exists a property called entropy S, which for systems in equilibrium states is an intrinsic property of the system, functionally related to the measurable coordinates which characterize the system. For reversible processes changes in this property may be calculated by the equation*

$$dS=dQ_{rev}/T \quad (2)$$

Where T is the absolute temperature of the system and Q_{rev} *is the reversible heat.*

Postulate 4: *The entropy change of any system and its surroundings, considered together, resulting from any real process is positive and approaches a limiting value of zero for any process that approaches reversibility.* (Second law of thermodynamics)."

Equations (1) and (2) apply for closed thermodynamic systems where the system and surroundings exchange energy only and matter is not exchanged. The mass of system or surroundings remain constant. If the system in thermodynamic equilibrium gains heat, it undergoes a spontaneous thermodynamic transformation until a new equilibrium is reached. In the process, heat and work are

DOI: https://doi.org/10.30564/jgr.v1i2.1007

exchanged between system and surroundings. Thermodynamic characteristics such as system pressure, temperature, and concentrations may be used as coordinates to define states of thermodynamic equilibrium. A thermodynamic transformation differentially displaced from equilibrium may be considered as a reversible transformation, in that the system may spontaneously return to its original characteristic coordinates when the cause of displacement ceases.

The biosphere as defined in the introduction section has a constant mass and exchanges energy with its surroundings. Therefore, it may be considered as a closed thermodynamic system and the first and second laws of thermodynamics thus apply. However, living matter is not considered in these thermodynamic relationships. The size of green matter is a coordinate of the biosphere thermodynamic system, and the energy exchanged resulting from the variation in its size is heat in transit that must be accounted for. Therefore, for the biosphere the first and second laws of thermodynamics should be revised to account for life in the biosphere. The subject is important because variation in the size of photosynthesis varies the heat content of the biosphere and changes climates. Similarly, deforestation is a reversed process of photosynthesis and it produces heat in the climate. Therefore, deriving the first and second laws of thermodynamics for the biosphere is important for research and society.

3. Revising the First and Second Laws of ThermoDynamics for the Biosphere

Publications [3,4] discuss the present state of photosynthesis understanding. It is a chemical reaction where water and carbon dioxide are converted into sugars, cellulose, carbohydrates and other plant constituents. Solar radiation and chlorophyll are required for the chemical reaction; it is an endothermic and non-spontaneous reaction. The solar energy is ultimately converted into chemical energy stored in plants' tissues, and biosphere subsystems loose this energy. While an increase in the size of photosynthesis removes heat from the biosphere, deforestation, decay, or combustion of green matter add heat to the biosphere because it is the reversed process of photosynthesis. If the chemical energy of green matter is indicated by Q_g, the first law of thermodynamics may be revised for the biosphere

$$dU=dQ_g-dW$$

Where U is now equal to the internal energy of the biosphere and W is the work exchanged in the biosphere. Not considered in this last equation radiative terms of biosphere subsystems. The reason is that life-dependent thermodynamic transformations are states differentially displaced from each other and the original starting thermodynamic state. Should this state be assumed to be in thermodynamic equilibrium, which is a reasonable assumption, radiative terms cancel out and may be eliminated from the equation. The same is true for all other thermodynamic states differentially displaced from the state of equilibrium.

The main biosphere subsystems are surface and atmosphere. Therefore

$$dU_s+dU_a=dQ_g-dW_a$$

Where the subscript "s" denotes surface and "a" for atmosphere. Because atmospheric air is surrounded by outer space whose pressure is negligible, variation in the internal energy of the atmosphere, dU_a, is equal to variation in its enthalpy, dH_a. The internal energy of the surface is equal to the heat of the surface Q_s. The work, W_a, is mainly potential energy of the atmosphere. Therefore, the first law simplifies.

$$dQ_s=dQ_g-(dW_a+dH_a)$$

The term (dW_a+dH_a) is energy exchanged between atmosphere and surface. It is equal to the opposite sign of the heat of carbon conversion to carbon dioxide, dQ_c, based on [5]. Consequently

$$dQ_s=dQ_c+dQ_g \quad (1\text{-}r)$$

The sum of surface heat and chemical energy of the biosphere is conserved.

Not mentioned in this form of the first law for the biosphere is the word surroundings. The reason is that the surroundings of the biosphere as defined in the introduction section are outer space and solid earth underneath the biosphere. Outer space is empty and no chemical energy, potential energy, or heat may be exchanged with outer space. The same is true for the solid earth; it is thick and rigid and the amount of energy exchanged with the solid earth may be neglected. The sign of dQ_g is negative if the size of the green matter increases and positive if the size decreases. Also, variation in the heat of carbon conversion dQ_c changes sign. It is positive when the content of carbon dioxide in the atmosphere increases and negative if the content decreases.

It should be noted that the chemical energy defined in this work is the energy associated with thermodynamic processes that exchange carbon in the biosphere. This energy interacts with the laws of thermodynamics according to Equation (1-r). Carbon free processes do not produce

 DOI: https://doi.org/10.30564/jgr.v1i2.1007

energy interaction and must exit the biosphere and climate system. Examples of these processes include but not limited to generation of earth's internal heat, transmission of energy of geological activities, and production of carbon-neutral energy.

On the other hand, the thermodynamic transformations caused by life are small displacements from each other. For instance, the present warming trend is less than one degree Kelvin in approximately 250 years. If compared with biosphere temperature of 288 K, the current climate change is in fact an incremental displacement from equilibrium. On an annual basis, biosphere transformations are infinitesimal processes. The same is true for all of past changes in climate. Even though they are infinitesimal displacements from equilibrium, they may not be assumed to be reversible, in that life adapts, evolves, and resists death and annihilation when environmental conditions are unfavorable. As a result, the second law of thermodynamics for the biosphere may be written as follows:

$$dS>0 \quad (2\text{-r})$$

The entropy of the biosphere increases with time.

Here, too, the word surroundings is removed for the same reasons discussed earlier. Equation (2-r) reveals that biosphere thermodynamic transformations are irreversible.

4. Discussion and Conclusions

The zeroth property of the living matter announces the resilience and strength of living matter as a continuous and unbreakable chain extending throughout eons. Living matter is indestructible; however, it may mutate or assume different shapes or forms. The first property on the other hand states that the size of life can never reach a steady value, it is inherently variable. As a result, the energy produced by life is energy transient in the biosphere that exchanges heat and work, Equation (1-r). The biosphere can never reach a thermodynamic equilibrium that characterizes thermodynamic systems of inert matter alone. Thermodynamic transformations driven by life in the biosphere are infinitesimal displacements around equilibrium. Yet, they are irreversible as the revised second law of thermodynamics for the biosphere reveals, Equation (2-r). This fundamental difference between thermodynamic systems where life is a variable and thermodynamic systems made of inert matter is of paramount importance. All life driven thermodynamic transformations have a direction. They are irreversible, and steady evolution of the biosphere is a natural outcome as a result that cannot come to a halt.

These thermodynamic conclusions for the biosphere are in agreement with the geological record. Life and biosphere has had a steady and uninterrupted evolution throughout geological time. The geological record is rich with overwhelming fossil samples supporting simultaneous evolution of life and biosphere. The age of surface rocks are predominately much younger than the age of the earth, and younger rocks are in the making at the present time. Living matter produced these younger rocks through biosynthesis of calcite, phosphate, and the large number of minerals that can be obtained from them such as chalk, gypsum, dolomite, fossil fuels, and others. Life has produced beautiful surface landscapes and majestic mountains made of sedimentary rocks around the world, thus testifying to the continuity, resilience, and power of living matter.

As Equation (1-r) reveals, variation in the size of life can change surface temperature and climates. The size of life depends on the size of the green matter. When the environmental conditions are favorable, an increase in the size of photosynthesis is an inherent nature of the green matter. The surface of the earth cools down, and a cooling cycle is initiated. These cooling periods are characterized of having severe cold and dry climates [6]. Colder surface temperature, reduced carbon dioxide content in the atmosphere, glaciers cover of land, and decreased water availability; all are unfavorable to life. The cooling cycles cannot continue indefinitely, there comes a time when the temperature in the biosphere is too cold for living matter. A large segment of life perishes as the cooling cycle progresses, which provides sediments for building continents and lands. Photosynthesis contracts in the process and the decay, oxidization, and combustion of living matter warms the biosphere and a warming or interglacial cycle is initiated. Environmental conditions become favorable for life to expand again. Only the species that adapt during the cooling cycle continue the journey of life. The warming and cooling cycles repeat throughout the geological history of the earth.

A warming cycle is much shorter than a cooling cycle. These cycles provide favorable conditions for life, and life tends to occupy the available spaces left from the devastation of the cooling cycle to the maximum extent and as quickly as possible. Figure 1 is a picture of Near Island, Alaska supporting this conclusion. The historical record [7] indicates that the island was not covered with dense spruce trees in the late eighteenth century. Apparently, climate change has provided favorable conditions for the trees to occupy the available spaces to the maximum extent including hard floors and solid rocks. There is, of course, death and decay of living matter during warming cycles as well. However, there is more growth than decay. Consequently, the mass of sediments pro-

DOI: https://doi.org/10.30564/jgr.v1i2.1007

duced in cooling cycles is considerably greater than that of warming cycles. These sediments ultimately accumulate at ocean floors and are accreted to the continent margins by tectonics. In addition, ocean floor spreading increases during warming cycles and decreases during cooling cycles [8, 9]. During cooling cycles, tectonics thus builds mountains and during warming cycles tectonics build valleys, and these mountain ranges are observed around the world. Figure 2 is a satellite picture of the Andes near Bolivia. The early mountains, farthest inland, are visible, apparently due to the building of new mountains westwards. These in turn may have arrested the destructive power of winds and water from the sea and preserved some of the mountains farther inland. Mountain ranges in other parts of the world reveal these cycles as well. Generally, they have been severely eroded by rain, glaciers, and rivers. The number and duration of the cycles may be roughly estimated using map scale and extrapolating to the subduction zone. Those that appear to be preserved mountain ranges may be used to calculate the number of complete interglacial and glacial cycles and age of the mountains. Using the image of Figure 2, the average length of a complete cycle is about 4.9 kilometers. At ocean floor spreading of nearly 8.0 centimeters annually [10], the average cycle duration is nearly 122 500 years. The number of cycles may be estimated by dividing the total distance to the subduction zone, about 1 000 kilometers, by cycle length, which yields to nearly 204 cycles. This is approximately the number of cycles needed to add all of the sedimentary or soft rocks to the platform of South America. The age of the rocks may be estimated as well by knowing the actual lineal length of the material accreted to the margins of this continent. The lineal length is hard to estimate with accuracy given that much of the mountains has eroded over the years and formed the surrounding landscapes. Assuming the angle of repose of the lithified sediments as 45 degrees, the original lineal length may be estimated at 2 830 kilometers. The Andes therefore began to form approximately 71 million years ago based on these simple observations. References [11, 12] estimate is between 40 and 60 million years ago.

The ongoing climate change supports the derived Equation (1-r). Present deforestation and fossil fuel burning has decreased the chemical energy of the biosphere. Simultaneously, the surface of the earth has accumulated heat. Clearly, the effects of the discussed properties of the living matter are embedded in the fabrics and tissues of the biosphere. These basic properties of life apply for small samples of single cell culture to complex organisms and animals and plants. The most relevant aspect of these properties is heat exchange in the biosphere, which interacts with the laws of thermodynamics. As a result, life has changed climates and surface geology.

5. Figures

Figure 1. Picture taken by the Author of Near Island off the east coast of Kodiak Island, Alaska, U.S.A. at 57.7900° N and 152.4072° W

Note: Spruce trees occupy the available spaces to the maximum extent.

Figure 2. Satellite image of the Andes near Bolivia, about -20° Latitude and -65° Longitude

Note: The mountain chains farther inland recorded the process with which sedimentary rocks were added or accreted by tectonics. Cooling cycles provided sedimentary rocks to build mountains, and the succeeding warming or interglacial periods left valleys behind. In the direction to the ocean, cycle fingerprints have been destroyed by the elements. The picture is a courtesy of U.S. Geological Survey.

Acknowledgements

My sincere thanks to the Editor, reviewers, and staff of the Journal of Geological Research for their review and comments. Mr. John Reinke is gratefully acknowledged for his review and constructive comments. Thanks to those who contributed directly or indirectly to this publication.

DOI: https://doi.org/10.30564/jgr.v1i2.1007

References

[1] Vernadsky V. I. The Biosphere. English version by Copernicus, Springer-Verlag: New York, U.S.A, 1926, 1998: 192.

[2] Perry R. H. and Green D. Perry's Chemical Engineers Handbook, 6th ed., Mc Graw-Hill, New York, U.S.A.. Ed. Crawford H. B. and Eckes B. E., Chapter 4, Thermodynamics, by Lin K. H., Van Ness H. C. and Abbott M. M., , 1984: 4-52+4-82.

[3] Anestis M. AP Biology, McGraw-Hill, New York, 2010: 359, Chapter 8, Photosynthesis: 73-84.

[4] Cain M. L., Bowman W. D. and Hacker S. D. Ecology, 3rd ed., Sinauer Associates, Inc., Sunderland, Massachusetts, U.S.A., 2014: 596. Chapter 4: 98-123; Chapter 10: 236-239.

[5] Swedan N. On the carbon cycle and its interactions with the biosphere, Russian Journal of Earth Sciences, 2019, 19, ES2007.
DOI:10.2205/2018ES000643

[6] Van der Hammen T. The Pleistocene Changes of Vegetation and Climate in Tropical South America, Journal of Biogeography, 1974, 1(1): 3-26.
DOI: 10.2307/3038066

[7] Black L. T. Russians in Alaska, University of Alaska Press, Fairbanks, Alaska, 2004: 328.

[8] Swedan N. H. Ridge Push Engine of Plate tectonics, Geotectonics, 2015, 49(4): 342-345.
DOI: 10.1134/S0016852115040081

[9] Swedan N. H. Association of Variations in the Dynamics of the Lithosphere with Sea Temperature, Journal of Geological Research, 2018, 1(1): 8-16.
DOI: https://doi.org/10.30564/jgr.v1i1.458

[10] Seton M., Gaina C., Müller R. D. and Heine C. Mid-Cretaceous seafloor spreading pulse: Fact or fiction? Geology, 2009,37(8): 687–690.
DOI: 10.1130/G25624A.1

[11] Graham A. The Andes: A Geological Overview from a Biological Perspective, Annals of the Missouri Botanical Garden, 2009, 6,(3): 371-385.
https://www.jstor.org/stable/40389940

[12] Berry E. W. The Age of the Bolivian Andes, Proc Natl AcadSci U S A, 1917,3(4): 283–285.
DOI: 10.1073/pnas.3.4.283

DOI: https://doi.org/10.30564/jgr.v1i2.1007

BILINGUAL PUBLISHING CO.
Pioneer of Global Academics Since 1984

Journal of Geological Research
https://ojs.bilpublishing.com/index.php/jgr-a

ARTICLE

Analysis and Discussion on Subway Construction Accidents from Geological Perspective

Yuanjian Lin[1,2] Jiangfeng Liu[1*] Ronghao Lv[1] Chenyi Sun[1] Zhendong Fan[1]

1.The State Key Laboratory for GeoMechanics and Deep Underground Engineering, and School of Mechanics and Civil Engineering, China University of Mining and Technology, Xuzhou 221116, China
2. School of Science, Nanchang Institute of Science and Technology, Nanchang 330108, China

ARTICLE INFO

Article history
Received: 24 May 2019
Accepted: 25 June 2019
Published Online: 30 July 2019

Keywords:
Subway station
Foundation pit
Collapse
Earthwork excavation

ABSTRACT

Several cave-in accidents often occur in subway construction, causing personnel and economic losses. This paper has carried on the statistics and analysis of some typical subway construction accidents in recent years. Taking the collapse accident of a subway station in Hangzhou as the engineering background, the causes of the collapse of the foundation pit were analyzed. The analysis found that groundwater, earthwork over-excavation, weak support design and inadequate monitoring are the main reasons. These factors should be highlighted in the construction of similar projects in the future to avoid similar tragedies.

1. Introduction

In recent years, China's urban rail transit construction has surged [1, 2]. By June 2019, 39 urban metro lines have been opened (sorted by the opening time of the first rail transit). With the development of metro lines in full swing all over the country, the metro construction accidents have arrived in quick succession, frequently ringing the alarm of safety [3, 4]. In the process of subway construction, the risk increases due to the properties of geotechnical complexity, unpredictable objects, the complicated construction procedures and equipment, concealment, and the permanence of construction period. Moreover, subway construction is a huge project, which needs a large number of workers. From its beginning, various risk factors have always existed. Once an accident occurs, it will cause serious casualties and property losses.

This paper gathers the typical accidents in China's subway construction in recent years, carries out corresponding analysis, especially from the perspective of hydrogeology and soil mechanics, and puts forward some thoughts and suggestions, hoping to provide some useful advice for the follow-up engineering design and construction.

2. Accident Statistics and Description

The author collects the subway construction accidents in China in recent years.

Accident 1: On September 21, 2004, the first phase construction of Shanghai Metro Line 9 was once in dan-

**Corresponding Author:*
Jiangfeng Liu,
The State Key Laboratory for GeoMechanics and Deep Underground Engineering, and School of Mechanics and Civil Engineering, China University of Mining and Technology, Xuzhou 221116, China;
Email: jeafliu@hotmail.com

 DOI: https://doi.org/10.30564/jgr.v1i2.1249

ger. A sewer was broken. The construction site was soaked in water, which caused the collapse of the ground of 700 square meters.

Accident 2: On the morning of March 28, 2007, a landslide occurred in Metro Line 10 near Suzhou Street in Beijing, and six builders were buried.

Accident 3: At 4 pm., December 17, 2007, the construction surface of Nanjing Metro Line 2 suddenly broke, which resulted in the collapse of the main road, covering an area of more than 300,000 square meters. Two trees over 10 meters high fell into the landslide. Fortunately, no casualties were caused.

Accident 4: On the afternoon of January 17, 2008, Guangzhou Metro Line 5 suddenly gushed water during construction and collapsed, resulting in a sudden subsidence of the ground near Shuangqiao Rd. under the approach span of the Pearl River Bridge. There was a large cave with an area of about 100 square meters and a depth of about 5 meters. No casualties were caused by the accident.

Accident 5: On April 1, 2008, when the construction team of Metro Line 3 in Longgang district of Shenzhen was casting concrete in place for pier, the mother slab suddenly collapsed with concrete pouring down. Five people were buried, resulting in three deaths and two injuries.

Accident 6: On November 15, 2008, a large-scale collapse occurred at the construction site of Hangzhou Metro Line 1, which caused the 75-meter pavement of Fengqing Avenue to collapse with a subsidence of 15 meters. 11 driving cars fell into the pit. The collapse of the soil outside caused the wall of foundation pit to be unstable. Then the supporting system collapsed, and a large amount of mud water flooded into the foundation pit. Four crumbling dilapidated buildings were forced to be demolished around the construction site. The residents within 500m were evacuated and transferred. 35 subway stations under construction in the city had to be suspended. This accident resulted in 21 deaths and 24 injuries, which is one of the most serious accidents in the history of metro construction in China. In this paper, the author will focus on the accident as the engineering background to analyze the cause of the accident and the measures taken, as shown in Figure 1.

Accident 7: On January 28, 2013, six collapses occurred successively near the construction site of Kangwang bus station, Liwan district of Guangzhou. Six shops collapsed and the cave-in area was about 690 square meters.

Accident 8: At 11 am, August 28, 2019, a road surface collapse occurred at the intersection of Jianguo North Road and Stadium Road in Hangzhou (Figure 2).

(a)

(b)

Figure 1. The construction accident at Xianghu Station of Hangzhou Metro Line 1, China.

Figure 2. The construction accident of Hangzhou Metro Line 5, China

DOI: https://doi.org/10.30564/jgr.v1i2.1249

3. Analysis and Discussion on the Causes of Accidents

3.1 Groundwater

In the construction process, the water in the soil has always been a nagging problem. Most of the accidents in geotechnical engineering are related to the water in the soil. In the construction process of subway stations, water is an important factor inducing accidents. According to the previous statistics, the construction accidents caused by improper water treatment account for about 21.4%.

Through the analysis of the accidents above, it is found that there are often water pipes or ground seepage around the foundation pit. For example, at the beginning of Accident 1, a small seepage appeared in the subway foundation pit, followed by a large-scale piping, and water with yellow sediment flooded into the subway foundation pit of Shanghai Metro Line 9. Meanwhile, the ground near the foundation pit began to fall, and the road about 50 meters long also collapsed in a large scale. This reason also applies in Accident 4 and Accident 6. According to the survey, the foundation soil near the Qiantang River is silty clay, and the groundwater level is high. In addition, the site is located in the main road, where traffic flow is relatively large. There are many large buses and trucks running on this road, which has brought impact on the western load-bearing wall of the foundation pit. In October 2007, a rare continuous rainfall occurred, which further increased the fluidity of soil under the foundation. Accident 8 was caused by water seepage in the construction of connecting passage of Hangzhou Metro Line 5, which resulted in pavement collapse and gas leakage.

In terms of geology and soil mechanics, due to the seepage of surface water and groundwater, the water content in the soil increases, that is, the self-weight of the soil increases, and the effective stress decreases. The seepage of water also causes a certain dynamic water pressure on the slope soil of foundation pit. Meanwhile, the accumulated water in the vertical cracks of the soil generates a certain hydrostatic pressure. On the other hand, the increase of water content in the soil causes lubrication among soil particles, and the internal friction angle of the original soil decreases greatly. As a result, the sliding force of foundation pit slope increases and the shear strength decreases, which eventually leads to the collapse of the slope and the subsidence and cave-in of the adjacent ground. Therefore, before the subway construction, it is necessary to focus on water factors which may cause accidents.

3.2 Design Factors

In Accident 6, the geology of the site is complicated, and it's rich in groundwater. Most of the soil layers are soft clay. The engineering work such as subway foundation pit excavation and shield tunneling is like drilling a hole in the cake, which is quite risky. The specificity of the soil mechanics parameters of groundwater and soft clay should be fully considered in the design. For the stability analysis of foundation pit, it is inappropriate to use consolidated undrained strength index and saturated unit weight for saturated clay. The design team has not paid enough attention to the particularity of soft clay.

When it comes to piles, walls and inner strut in deep soft soil areas, stability in depth must be considered, including pile and wall settlement, upheave and "skirting" damage, which should be strictly calculated by various methods. If it cannot meet the requirements, it should deepen the depth of pile and wall into soil or reinforce the passive area. In Accident 6, the project design has not paid enough attention to this, and no passive zone reinforcement has been carried out.

3.3 Construction Factors

The quality of a project ultimately depends on the quality control of construction. One of the most important reasons in accident 6 is that the steel support booster was not added enough, which made the bearing capacity of the protective wall insufficient. Generally speaking, the booster should be added to more than 200 tons, even 300 tons in geological conditions such as Hangzhou, but in terms of the accident site, it is certainly not enough.

In addition, the protective wall of the west subway section underwent tremendous deformation. The sliding of the protective wall had occurred sometime before the accident. Earlier, many on-site construction workers had also noticed cracks on the wall, but no measures were taken. Besides, serious road subsidence and multiple cracks occurred one month ago, which actually reflected the change of soil mass, but it was still ignored as a result of excessive traffic flow by the construction team. Moreover, in the construction process, the foundation pit was seriously over-excavated. The supporting system had serious defects. The steel pipe support was not timely erected, and the cushion was not timely poured, either.

Because of the short construction period, many details were neglected in order to rush to meet the deadlines, which actually caused management omissions. For example, in the subway station, if the open excavation starts, the multi-section construction method must be strictly implemented, and every 20 meters should be segmented.

DOI: https://doi.org/10.30564/jgr.v1i2.1249

However, after the accident, it was found that the interval between sections was 60 meters. Although it is difficult to establish a direct causal relationship between the shortening of construction period and cave-in accidents, facts show that the shortening of construction period indirectly promotes the occurrence of accidents to a certain extent, so that dangers which could have been discovered are ignored intentionally or unintentionally.

3.4 Monitoring Measurement

There must be an omen before the foundation pit collapses. The monitoring data of the foundation pit will certainly give an alarm according to the daily reports. General monitoring items include horizontal displacement and settlement monitoring, inclinometer monitoring, stress monitoring, earth pressure monitoring, water level monitoring.

In Accident 6, the soil near the station was relatively soft with high fluidity. The pressure caused by the traffic flow on the west Fengqing Avenue led to the soil layer below moving toward the subway construction site. In addition, the previous rainfall caused the surge of river in the east. The softer soil also increased the mobility of the soil layer. Under this background, monitoring data such as horizontal displacement, earth pressure and water level change should be able to detect the abnormal situation in advance and send out an alarm so that the construction team could take corresponding measures. But in that situation, this was obviously not well tackled.

4. Some Reflections

(1) Make a good pre-construction survey. With the deepening excavation of foundation pit, the risk of confined water is also increasing, which can easily break through the weak stratum, resulting in piping and drift sand. Therefore, a good survey should be made before the construction of foundation pit. The features of the site, the adjacent aquifers, and the hydraulic relations between aquifers and surface water should be clarified. Then make a design of dewatering.

(2) In the engineering design, it's inappropriate to use consolidated undrained strength index and saturated unit weight to calculate the strength of groundwater subsoil, to analyze the stability and to check the bottom upheave. The highly sensitive soft soil was not given enough attention and no effective measures were taken. A mistake was made at the time when Fengqing Avenue was not closed. The checking calculation of pit overload based on consolidated undrained strength was also dangerous. In addition, according to the disturbance degree of the subsoil, the disturbed soil is strengthened by layers.

(3) In the construction process, it is necessary to ensure the construction quality of the underground continuous wall, and dewatering should be carried out according to the design.

(4) Strengthen monitoring and measurement. During the excavation of the foundation pit, it is necessary to ensure the safety of the pit, the surrounding buildings and underground pipelines. Therefore, in the construction process, informationized monitoring of foundation pit and its surroundings should be strengthened, and the monitoring data should be promptly sent to the construction team.

(5) Eliminate man-made accidents from institutional mechanisms. Eliminate illegal subcontracting, and set the construction period from a scientific development perspective, which cannot be guided by the leadership's thinking. Many metro projects are constructed underground, which is highly risky. Therefore, a more complete technical support system and a stricter monitoring and risk management should be required.

References

[1] Liu JF, Qi TY, Wu ZR. Analysis of ground movement due to metro station driven with enlarging shield tunnels under building and its parameter sensitivity analysis. Tunnelling and Underground Space Technology, 2012, 28(3): 287–296

[2] Tan J , Yang L , Grimmond C S B , et al. Urban Integrated Meteorological Observations: Practice and Experience in Shanghai, China. Bulletin of the American Meteorological Society, 2015, 96(1): 85-102.

[3] Chen Y, Hu Q, Chen R. Soil disturbance by the collapse of retaining wall for a pit excavation and the induced additional settlement:a case study of Hangzhou Metro Xianghu Station. China Civil Engineering Journal, 2014, 47(7): 110-117.

[4] Cui Q L , Wu H N , Shen S L , et al. Chinese karst geology and measures to prevent geohazards during shield tunnelling in karst region with caves[J]. Natural Hazards, 2015, 77(1): 129-152.

DOI: https://doi.org/10.30564/jgr.v1i2.1249

Author Guidelines

This document provides some guidelines to authors for submission in order to work towards a seamless submission process. While complete adherence to the following guidelines is not enforced, authors should note that following through with the guidelines will be helpful in expediting the copyediting and proofreading processes, and allow for improved readability during the review process.

Ⅰ. Format

- Program: Microsoft Word (preferred)
- Font: Times New Roman
- Size: 12
- Style: Normal
- Paragraph: Justified
- Required Documents

Ⅱ. Cover Letter

All articles should include a cover letter as a separate document.

The cover letter should include:

- Names and affiliation of author(s)

The corresponding author should be identified.

Eg. Department, University, Province/City/State, Postal Code, Country

- A brief description of the novelty and importance of the findings detailed in the paper

Declaration

v Conflict of Interest

Examples of conflicts of interest include (but are not limited to):

- Research grants
- Honoria
- Employment or consultation
- Project sponsors
- Author’s position on advisory boards or board of directors/management relationships
- Multiple affiliation
- Other financial relationships/support
- Informed Consent

This section confirms that written consent was obtained from all participants prior to the study.

- Ethical Approval

Eg. The paper received the ethical approval of XXX Ethics Committee.

- Trial Registration

Eg. Name of Trial Registry: Trial Registration Number

- Contributorship

The role(s) that each author undertook should be reflected in this section. This section affirms that each credited author has had a significant contribution to the article.

1. Main Manuscript

2. Reference List

3. Supplementary Data/Information

Supplementary figures, small tables, text etc.

As supplementary data/information is not copyedited/proofread, kindly ensure that the section is free from errors, and is presented clearly.

Ⅲ. Abstract

A general introduction to the research topic of the paper should be provided, along with a brief summary of its main results and implications. Kindly ensure the abstract is self-contained and remains readable to a wider audience. The abstract should also be kept to a maximum of 200 words.

Authors should also include 5-8 keywords after the abstract, separated by a semi-colon, avoiding the words already used in the title of the article.

Abstract and keywords should be reflected as font size 14.

Ⅳ. Title

The title should not exceed 50 words. Authors are encouraged to keep their titles succinct and relevant.

Titles should be reflected as font size 26, and in bold type.

Ⅳ. Section Headings

Section headings, sub-headings, and sub-subheadings should be differentiated by font size.

Section Headings: Font size 22, bold type

Sub-Headings: Font size 16, bold type

Sub-Subheadings: Font size 14, bold type

Main Manuscript Outline

Ⅴ. Introduction

The introduction should highlight the significance of the research conducted, in particular, in relation to current state of research in the field. A clear research objective should be conveyed within a single sentence.

Ⅵ. Methodology/Methods

In this section, the methods used to obtain the results in the paper should be clearly elucidated. This allows readers to be able to replicate the study in the future. Authors should ensure that any references made to other research or experiments should be clearly cited.

Ⅶ. Results

In this section, the results of experiments conducted should be detailed. The results should not be discussed at length in

this section. Alternatively, Results and Discussion can also be combined to a single section.

Ⅷ. Discussion

In this section, the results of the experiments conducted can be discussed in detail. Authors should discuss the direct and indirect implications of their findings, and also discuss if the results obtain reflect the current state of research in the field. Applications for the research should be discussed in this section. Suggestions for future research can also be discussed in this section.

Ⅸ. Conclusion

This section offers closure for the paper. An effective conclusion will need to sum up the principal findings of the papers, and its implications for further research.

Ⅹ. References

References should be included as a separate page from the main manuscript. For parts of the manuscript that have referenced a particular source, a superscript (ie. [x]) should be included next to the referenced text.

[x] refers to the allocated number of the source under the Reference List (eg. [1], [2], [3])

In the References section, the corresponding source should be referenced as:

[x] Author(s). Article Title [Publication Type]. Journal Name, Vol. No., Issue No.: Page numbers. (DOI number)

Ⅺ. Glossary of Publication Type

J = Journal/Magazine

M = Monograph/Book

C = (Article) Collection

D = Dissertation/Thesis

P = Patent

S = Standards

N = Newspapers

R = Reports

Kindly note that the order of appearance of the referenced source should follow its order of appearance in the main manuscript.

Graphs, Figures, Tables, and Equations

Graphs, figures and tables should be labelled closely below it and aligned to the center. Each data presentation type should be labelled as Graph, Figure, or Table, and its sequence should be in running order, separate from each other.

Equations should be aligned to the left, and numbered with in running order with its number in parenthesis (aligned right).

Ⅻ. Others

Conflicts of interest, acknowledgements, and publication ethics should also be declared in the final version of the manuscript. Instructions have been provided as its counterpart under Cover Letter.

BILINGUAL PUBLISHING CO.
Pioneer of Global Academics Since 1984

Journal of Geological Research

Aims and Scope

Journal of Geological Research publishes original research papers that offers a rapid review and publication that freely disseminates research findings in all areas of Geology including Petrology, Mineralogy, Engineering Geology, Regional Geology and more. The Journal focuses on innovations of research methods at all stages and is committed to providing theoretical and practical experience for all those who are involved in these fields.

Journal of Geological Research aims to discover innovative methods, theories and studies in all aspects of Geology by publishing original articles, case studies and comprehensive reviews.

The scope of the papers in this journal includes, but is not limited to:

- Petrology
- Mineralogy
- Geochemistry
- Stratigraphy
- Deposit Geology
- Structural Geology
- Economic Geography
- Hydrogeology
- Engineering Geology
- Regional Geology

Bilingual Publishing Co. (BPC)

Tel:+65 65881289

E-mail:contact@bilpublishing.com

Website:www.bilpublishing.com

About the Publisher

Bilingual Publishing Co. (BPC) is an international publisher of online, open access and scholarly peer-reviewed journals covering a wide range of academic disciplines including science, technology, medicine, engineering,education and social science. Reflecting the latest research from a broad sweep of subjects, our content is accessible worldwide – both in print and online.

BPC aims to provide an analytics as well as platform for information exchange and discussion that help organizations and professionals in advancing society for the betterment of mankind. BPC hopes to be indexed by well-known databases in order to expand its reach to the science community, and eventually grow to be a reputable publisher recognized by scholars and researchers around the world.

BPC adopts the Open Journal Systems, see on http://ojs.bilpublishing.com

Database Inclusion

Asia & Pacific Science Citation Index

Creative Commons

China National Knowledge Infrastructure

Google Scholar

Crossref

MyScienceWork

Bilingual Publishing Co. is a company registered in Singapore in 1984, whose office is at 12 Eu Tong Sen Street, #08-169, Singapore 059819, enjoying a high reputation in Southeast Asian countries, even around the world.

Tel:+65 65881289
E-mail:contact@bilpublishing.com
Website:www.bilpublishing.com

BILINGUAL
PUBLISHING CO.
Pioneer of Global Academics Since 1984

ISSN 2630-4961
02
9 772630 496195